AFRL-AFOSR-VA-TR-2022-0134

Nanoscale Pyroelectric Hybrid Materials Undergoing Structural Phase Transition

Jian Shi
RENSSELAER POLYTECHNIC INST TROY NY
100 8TH STREET
TROY, NY,
US

04/24/2022
Final Technical Report

Air Force Research Laboratory
Air Force Office of Scientific Research
Arlington, Virginia 22203
Air Force Materiel Command

REPORT DOCUMENTATION PAGE

PLEASE DO NOT RETURN YOUR FORM TO THE ABOVE ORGANIZATION.

1. REPORT DATE	2. REPORT TYPE	3. DATES COVERED	
20220424	Final	START DATE 20180115	END DATE 20210114

4. TITLE AND SUBTITLE
Nanoscale Pyroelectric Hybrid Materials Undergoing Structural Phase Transition

5a. CONTRACT NUMBER	5b. GRANT NUMBER	5c. PROGRAM ELEMENT NUMBER
	FA9550-18-1-0116	61102F
5d. PROJECT NUMBER	**5e. TASK NUMBER**	**5f. WORK UNIT NUMBER**

6. AUTHOR(S)
Jian Shi

7. PERFORMING ORGANIZATION NAME(S) AND ADDRESS(ES)
RENSSELAER POLYTECHNIC INST TROY NY
100 8TH STREET
TROY, NY
US

8. PERFORMING ORGANIZATION REPORT NUMBER

9. SPONSORING/MONITORING AGENCY NAME(S) AND ADDRESS(ES)	10. SPONSOR/MONITOR'S ACRONYM(S)	11. SPONSOR/MONITOR'S REPORT NUMBER(S)
Air Force Office of Scientific Research 875 N. Randolph St. Room 3112 Arlington, VA 22203	AFRL/AFOSR RTB1	AFRL-AFOSR-VA-TR-2022-0134

12. DISTRIBUTION/AVAILABILITY STATEMENT
A Distribution Unlimited: PB Public Release

13. SUPPLEMENTARY NOTES

14. ABSTRACT
This project explores the fundamental relation between pyroelectricity and structures/lattice dynamics/electron-phonon renormalization of nanoscale materials. Over this project, we have showed that (1) electron-phonon renormalization plays a substantial role in pyroelectricity; (2) electron-phonon renormalization can be tuned drastically by the dimensionality of the nanoscale pyroelectric materials including polar oxides and chalcogenides; (3) through dimensionality engineering, giant pyroelectric coefficients and figures of merits can be received; (4) the thermally-induced phase transition of VO2 could drastically modify the felxo-photovoltaic behaviors of strain gradient-engineered chalcogenides; (5) the phase transition of VO2 can induce significant strain in halide leading to structural phase transition of halide.

15. SUBJECT TERMS

16. SECURITY CLASSIFICATION OF:			17. LIMITATION OF ABSTRACT	18. NUMBER OF PAGES
a. REPORT U	b. ABSTRACT U	c. THIS PAGE U	UU	25

19a. NAME OF RESPONSIBLE PERSON	19b. PHONE NUMBER *(Include area code)*
ALI SAYIR	426-7236

Final Performance Report

Principal Investigator: Jian Shi

Rensselaer Polytechnic Institute

Email: shij4@rpi.edu

Phone: 573-239-8872

Title of the project: Nanoscale Pyroelectric Hybrid Materials with Structural Phase Transition

Grant #: FA9550-18-1-0116

Program officer: Dr. Ali Sayir, Aerospace Materials for Extreme Environments, AFOSR/RTB1, (703) 588-7236, ali.sayir.2@us.af.mil

Reporting Period: 01/15/2018-01/14/2022

Abstract:

This project explores the fundamental relation between pyroelectricity and structures/lattice dynamics/electron-phonon renormalization of nanoscale materials. Over this project, we have showed that (1) electron-phonon renormalization plays a substantial role in pyroelectricity; (2) electron-phonon renormalization can be tuned drastically by the dimensionality of the nanoscale pyroelectric materials including polar oxides and chalcogenides; (3) through dimensionality engineering, giant pyroelectric coefficients and figures of merits can be received; (4) the thermally-induced phase transition of VO_2 could drastically modify the felxo-photovoltaic behaviors of strain gradient-engineered chalcogenides; (5) the phase transition of VO_2 can induce significant strain in halide leading to structural phase transition of halide.

As attached is the unpublished manuscript on the role electron-phonon renormalization on pyroelectricity. This manuscript is under review.

Publications supported by this project:

1. Wang Y, Sun X, Chen Z, Cai Z, Zhou H, Lu TM, Shi J. Defect-engineered epitaxial VO2±δ in strain engineering of heterogeneous soft crystals. Science Advances 2018, 4, eaar3679.
2. Chen J, Mao W, Ge B, Wang J, Ke X, Wang V, Wang Y, Döbeli X, Geng W, Matsuzaki H, Shi J, Jiang Y, Revealing the role of lattice distortions in the hydrogen-induced metal-insulator transition of SmNiO3. Nat. Commun. 2019, 10 (1), 694.
3. Li L, Li Z, Yoshimura A, Sun C, Wang T, Chen Y, Chen Z, Littlejohn A, Xiang Y, Hundekar P, Bartolucci S, Shi J, Shi S-F, Meunier V, Wang G-C, Koratkar N, Vanadium disulfide flakes with nanolayered titanium disulfide coating as cathode materials in lithium-ion batteries. Nat. Commun. 2019, 10 (1), 1764
4. Jiang J, Sun X, Chen X, Wang B, Chen Z, Hu Y, Guo G, Zhang L, Ma Y, Gao L, Zheng F, Jin L, Chen M, Ma Z, Zhou Y, Padture NP, Beach K, Terrones H, Shi Y, Gall D, Lu TM, Wertz E, Feng J, Shi J, Carrier lifetime enhancement in halide perovskite via remote epitaxy. Nat. Commun. 2019, 10, 4145.
5. Guo Y, Sun X, Jiang J, Wang B, Chen X, Yin Y, Qi W, Gao L, Zhang L, Lu Z, Jia R, Pendse S, Hu Y, Chen Z, Wertz E, Gall D, Feng J, Lu TM, Shi J, A reconfigurable remotely epitaxial VO2 electrical heterostructure. Nano Lett., 2020, 20, 33.
6. Hu Y, Florio F, Chen Z, Phelan W. A., Siegler M. A., Zhou Z, Guo Y, Hawks R, Jiang J, Feng J, Zhang L, Wang B, Wang Y, Gall D, Palermo E. F., Lu Z, Sun X, Lu T-M, Zhou H, Ren Y, Wertz E, Sundararaman R, Shi J, A chiral switchable photovoltaic ferroelectric 1D perovskite. Science Advances, 2020, 6, eaay4213.

7. Pendse S, Jiang J, Zhang L, Guo Y, Chen Z, Hu Y, Lu Z, Li S, Feng J, Lu TM, Shi J, Tuning phase transition kinetics via van der Waals epitaxy of single crystalline VO2 on hexagonal-BN, J. Cryst. Growth, 125699, 2020
8. Chen J, Mao W, Gao L, Yan F, Yajima T, Chen N, Chen Z, Dong H, Ge B, Zhang P, Cao X, Wilde M, Jiang Y, Terai T, Shi J, Electron-doping Mottronics in strongly correlated perovskite. Adv. Mater., 2019, 1905060.
9. Pendse S, Jiang J, Guo Y, Zhang L, Chen Z, Lu Z, Wang Y, Hu Y, Li S, Feng J, Lu TM, Sun YY, Shi J, Unit-Cell-Thick Oxide Synthesis by Film-Based Scavenging. J. Phys. Chem. C, 2020, 124, 8394.
10. Chen Z, Hu Y, Zhang L, Jiang J, Hawks R, Shi J, Photo-active electrically switchable van der Waals semiconductor NbOI2. Appl. Phys. Lett., 2021, 119, 033103.
11. Barringer Z, Jiang J, Shi X, Schold E, Pateras A, Cipiccia S, Rau C, Shi J, Fohtung E, Imaging Defects in Vanadium (III) Oxide Nanocrystals using Bragg Coherent Diffractive Imaging. CrystEngComm, 2021, 23, 6239-6244.
12. Jia R, Kum H-S, Sun X, Guo Y, Wang B, Fang P, Jiang J, Gall D, Lu T-M, Washington M, Kim J, Shi J, van der Waals Epitaxy and Remote Epitaxy of LiNbO3 Thin Films by Pulsed Laser Deposition. J. Vac. Sci. Technol. A, 2021, 39, 040405 (EDITORS' PICK).
13. Jiang J, Chen Z, Hu Y, Xiang Y, Zhang L, Wang Y, Wang GC, Shi J, Flexo-Photovoltaic Effect in MoS2. Nature Nanotechnology, 2021, 16, 894–901.
14. Zhang L, Jiang J, Cai Y, Yao S, Azhar B, Chen Z, Hu Y, Pendse S, Guo Y, Jia R, Tian Z, Sun C, Liao P, and Shi J, Doping-Enabled Reconfigurable Strongly Correlated Phase in a Quasi-2D Perovskite. J. Phys. Chem. Lett, 2021, 12, 21, 5091–5098.
15. Guo Y, Goodge B, Zhang L, Jiang J, Chen Y, Kourkoutis L, Shi J, Unit-cell-thick domain in free-standing quasi-2D ferroelectric material. Phys. Rev. Mater., 2021, 5, 044403 (EDITORS' SUGGESTION).

Giant Pyroelectricity in Nanomembranes

Jie Jiang[#,Δ,*], Lifu Zhang[#,Δ], Chen Ming[¤], Hua Zhou[^], Pritom Bose[Δ], Yuwei Guo[Δ], Yang Hu[Δ], Baiwei Wang[Δ], Zhizhong Chen[Δ], Ru Jia[Δ], Saloni Pendse[Δ], Yu Xiang[$], Yaobiao Xia[$], Zonghuan Lu[$], Xixing Wen[$], Yao Cai[◊], Chengliang Sun[◊], Gwo-Ching Wang[$], Toh-Ming Lu[$], Daniel Gall[Δ], Yi-Yang Sun[¤], Nikhil Koratkar[Δ], Edwin Fohtung[Δ], Yufeng Shi[Δ,*], Jian Shi[Δ,%,*]

[Δ]Department of Materials Science and Engineering, Rensselaer Polytechnic Institute, Troy, New York 12180, USA

[¤]State Key Lab of High-Performance Ceramics and Superfine microstructure, Shanghai Institute of Ceramics, Chinese Academy of Sciences, Shanghai, PR China

[^]X-ray Science Division, Advanced Photon Source, Argonne National Laboratory, Lemont, IL 60439, USA

[$]Department of Physics, Applied Physics and Astronomy, Rensselaer Polytechnic Institute, Troy, New York 12180, USA

[◊]The Institute of Technological Sciences, Wuhan University, Wuhan 430072, PR China

[%]Center for Materials, Devices, and Integrated Systems, Rensselaer Polytechnic Institute, Troy, NY 12180, USA

Abstract

Electron-phonon renormalization in solids is often viewed negligible but has been theorized deterministic in evaluating physical properties like band gap[1]. Early in 1945, Born proposed a quantum theory of "true" pyroelectricity concluding that the temperature-dependent electron-phonon renormalization must be the source of polarization change[2]. Later in 1975, Szigeti complemented Born's theory by taking the internal strain into account[3]. Until recently, the contribution of electron-phonon renormalization to pyroelectricity was only emphasized theoretically[4]. When pyroelectric materials approach the two-dimensional crystalline limit, how electron-phonon renormalization influences pyroelectricity was also a mystery. In this work, with three model pyroelectric materials whose bonding characters along the out-of-plane direction vary from van der Waals (In_2Se_3), quasi-van der Waals ($CsBiNb_2O_7$) to ionic/covalent (ZnO), we experimentally reveal the dimensionality effect on pyroelectricity and the relation between electron-phonon renormalization and pyroelectricity. We find that for all three materials when the thickness of freestanding sheets become small their pyroelectric coefficients increase rapidly. It is found that the material with chemical bonds along the out-of-plane direction exhibits the greatest dimensionality effect. Experimental evidences of pyroelectric coefficients, phonon dynamics and Debye-Waller factors and molecular dynamic simulations all show that the increased phonon dynamics in crystals with reduced thickness may play an important role. Our finding would not only stimulate fundamental study on pyroelectricity in ultrathin materials and inspire technological development for potential pyroelectric applications in thermal imaging and energy harvesting, but also reveal the importance of electron-phonon coupling crucial for nanomembrane electronics[5].

Mechanism of pyroelectricity and dimensionality effect

Pyroelectricity is the temperature fluctuation (temporal temperature gradient) response of the spontaneous polarization in pyroelectric materials. It has been widely utilized in thermal imagings[6,7], sensors[8-10], nanogenerators[11], energy harvestors[11-14], hydrogen generation[15-17] and nuclear fusion[18,19]. One of the unique advantages of pyroelectric devices is the ultrafast response down to picoseconds[20]. The understanding of polarization and pyroelectricity based on the classic Clausius-Mossotti model[21] with the assumption of identifiable "polarization centers" is not precise, because the electronic charge in a real crystal has a periodic continuous distribution instead of localized contributions. Later the development of modern theory of polarization (Berry phase polarization) considers the electron cloud distribution but it focuses on the contribution of static lattice[21]. The pyroelectric coefficient p, measuring the "ability" of polarization change with fixed temperature fluctuation, is mainly contributed by the primary pyroelectricity p_1 (at constant external strain but vibrating lattice, so-called "clamped-lattice" pyroelectricity) and the secondary pyroelectricity p_2 (combined effects of piezoelectricity and thermal expansion)[7]. Here, we only focus on p_1 due to the minor contribution of p_2 in most crystals[7].

In 1945, Born found a quantum mechanical solution of the primary pyroelectricity out of harmonic vibrations of ions[2]. Born's theory can be understood by the renormalization of electronic states due to electron-phonon interactions. The redistribution of the electron cloud (when $dT/dt > 0$) is shown in Fig. 1b with respect to the original state (when $dT/dt = 0$) in Fig. 1a. With the Taylor expansion of the electron-phonon interaction $V(r - l - u_l)$ about the atomic displacements $u_l = 0$ with respect to their average position l (r denotes the position of electron), the Hamiltonian is[1,22]

$$\mathcal{H} = \mathcal{H}_0 + \mathcal{H}_1 + \mathcal{H}_2 = \mathcal{H}_0 + \sum_l u_l \nabla_l V(r-l) + \frac{1}{2}\sum_l u_l u_l \nabla_l \nabla_l V(r-l), \quad (1)$$

where $\mathcal{H}_0$ is given by neglecting u_l and $\nabla_l V(r - l)$ is the change in electron-lattice potential per unit displacement of atom. In the harmonic approximation, $\mathcal{H}_1$ is dropped because the thermal averaging of u_l is vanished. $\mathcal{H}_2$ induces a second-order redistribution of the electron cloud, which is known as the Debye-Waller (DW) term. The DW term represents one electron interacting with two phonons once. This electron-phonon renormalization is related to the mean square displacement $\langle {u_l}^2 \rangle$, contributing to pyroelectricity. For example, in pyroelectrics, the electron clouds could become more delocalized when $dT/dt > 0$ (Fig. 1b) than their original states when $dT/dt = 0$ (Fig. 1a).

Later in 1975, Szigeti complemented Born's theory by taking an anharmonic-potential term (also known as the internal strain) into account and revealed its contribution to the primary pyroelectricity[3]. Thus, the overall primary pyroelectric coefficient is expressed as[3,4,23]:

$$p_1 = {p_1}^{(1)} + {p_1}^{(2)} = \sum_a \frac{\partial P_S}{\partial Q_a}\frac{d\langle Q_a \rangle}{dT} + \sum_j \frac{\partial^2 P_S}{\partial {Q_j}^2}\frac{d\langle {Q_j}^2 \rangle}{dT}, \quad (2)$$

where P_S is the spontaneous polarization, Q_a is the active normal coordinate producing polarization in the direction of P_S, Q_j is the normal coordinate, ${p_1}^{(1)}$ is the first-order primary pyroelectric coefficient due to the rigid-ion displacement (the internal strain term) and ${p_1}^{(2)}$ is the second-order contribution due to the electron-phonon renormalization. An anharmonic-potential profile of an ion and its displacement when $dT/dt > 0$ are shown between Fig. 1a and Fig. 1c. The displacements of ions contributed solely from ${p_1}^{(1)}$ are indicated in Fig. 1c.

Recently, the microscopic mechanisms of the pyroelectric effects in three- and two-dimensional (3D and 2D) materials have been revisited based on first-principles calculations[4,24]. The contribution of the electron-phonon renormalization to pyroelectricity, which has been traditionally viewed as negligible, is found to be important. Theoretically, the 2D crystalline long-range order cannot exist within the thermodynamic limit, which is argued by Peierls based on the harmonic approximation[25], Landau based on an order-parameter expansion[26], and Hohenberg, Mermin and Wagner based on rigorous inequalities[27-30]. Topological defects like dislocation pairs may stabilize a quasi-ordered (hexatic) phase and an unusual phase transition might occur in 2D systems, known as the Kosterlitz-Thouless-Halperin-Nelson-Young (KTHNY) theory[31-33]. A dimensional limit of a long-range ordered crystalline phase had been expected[34]. But the discovery of graphene[35] and monolayer crystalline oxides[36,37] seem to defy these theorems. Debates on whether these 2D crystals can be approximated to Hohenberg-Mermin-Wagner's or KTHNY's

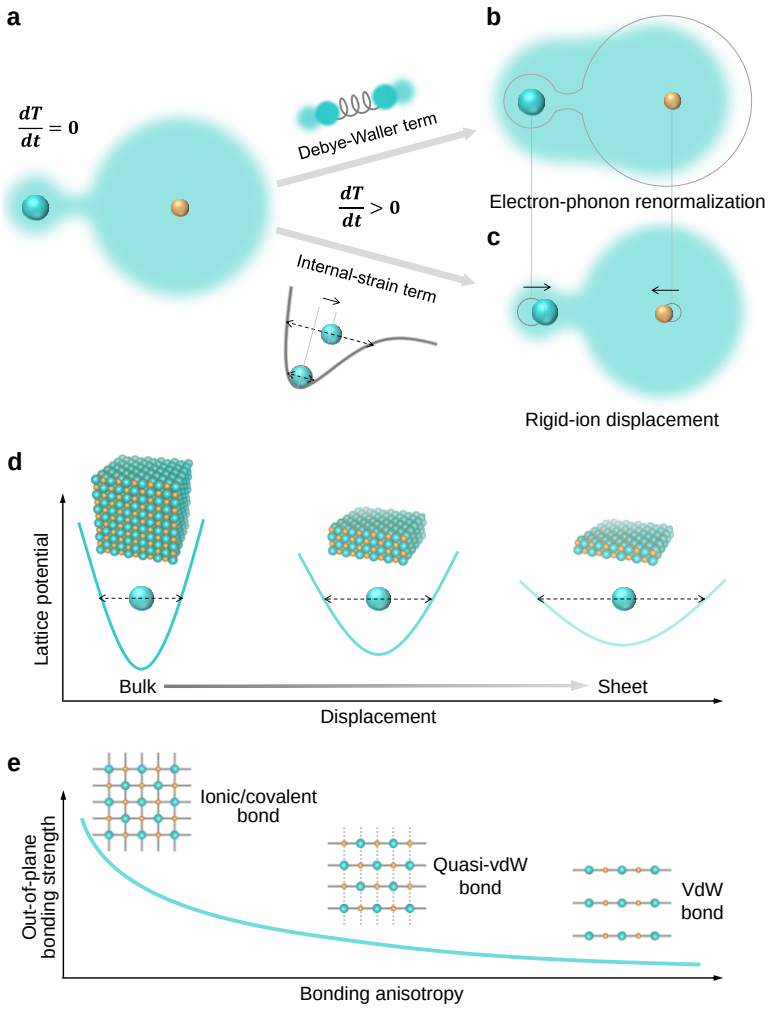

Fig. 1 | Schematics of the microscopic mechanism of the primary pyroelectricity and dimensionality effect. **a**,**b**,**c**, Original state (**a**) and solely contributed from $p_1^{(2)}$ (**b**) and $p_1^{(1)}$ (**c**) of ions and electron clouds (fuzzy cyan) in a crystal lattice. The schematic between (**a**) and (**b**) represents the Debye-Waller term that contributes to the electron-phonon renormalization. The lattice potential profile of an ion between (**a**) and (**c**) shows the origin of rigid-ion displacement (internal-strain term). Positive ions are in cyan and negative ones are in orange. Black arrows represent the direction of the ion displacement. The dashed shape in **b** and circles in **c** represent the original shape of the electron cloud and positions of ions, respectively. Dashed arrows represent the amplitude of the ion vibration. **d**, Schematics of lattice potential profiles and ion displacements as the thickness of crystal decreases (from bulk to sheet) based on Hohenberg-Mermin-Wagner's theorem. **e**, Schematic plot of out-of-plane bonding strength as a function of bonding anisotropy in different materials. Insets show the lattices of materials with ionic/covalent bond, quasi-vdW bond and vdW bond. The out-of-plane bonding strength decreases and bonding anisotropy increases from ionic/covalent crystal, quasi-vdW crystal to vdW crystal.

model have been raised. Nevertheless, it is generally observed that the thermodynamic-relevant long-range order (e.g., phonon) becomes less stable when approaching 2D thereby affecting material properties[38-43].

For the purpose of illustration, in an extreme case, here, Hohenberg-Mermin-Wagner's theorem is applied to estimate the possible dimensionality effect of $\langle {u_l}^2 \rangle$. Hohenberg-Mermin-Wagner's theorem gives a finite value of $\langle {u_l}^2 \rangle$ in 3D while an infinite value in 2D, which is described in Supplementary Discussion 1. The physical reason leading to such prediction is that in 3D system the atomic displacements are restrained by atoms from all directions while in 2D such constriction is absent. Thus, it

is naturally expected that as the thickness of a crystal decreases, there would be less restrictions for atoms to displace. In this scenario, $\langle {u_i}^2 \rangle$ could become larger (Fig. 1d). Hence, the pyroelectric behavior (${p_1}^{(2)}$) in 2D and freestanding nanomembranes would be very different from that in 3D.

Though conceptually illustrative, Hohenberg-Mermin-Wagner's analysis takes into account some significant assumptions such as single element. Real materials exhibit further complexity. For example, for a non-van der Waals (non-vdW) 3D material (e.g., ZnO) with strong chemical bond, thinning it down by removing the strong constrictions along the out-of-plane direction would have much more impacts on its phonon dynamics and phase stability than a vdW material (e.g., In_2Se_3) (Fig. 1e). In fact, it has been theoretically predicted that freestanding monolayer wurtzite ZnO should not exist[44], while monolayer In_2Se_3 has been experimentally demonstrated widely[45]. Thus, we expect that the bonding nature along the out-of-plane direction in real materials would influence the dimensionality effect of pyroelectricity: more pronounced dimensionality effect is expected in non-vdW system. The dimensionality effect of freestanding nanomembranes should be distinguished from the scenario in epitaxial films which are tightly bonded on the underlying substrate with the lattice dynamics (e.g., coefficients of thermal expansion) of epilayers largely determined by the substrates. Such dimensionality effect is also different from the pyroelectricity with the dipole moment along the out-of-plane direction induced by inversion symmetry breaking at the surface or interface of materials[46,47].

In this study, we experimentally investigate the dimensionality effect of pyroelectricity in vdW, quasi-vdW, and ionic/covalent pyroelectric materials. We choose β'-In_2Se_3, $CsBiNb_2O_7$ (CBNO) and ZnO as representative pyroelectric materials with vdW, quasi-vdW and ionic/covalent bonds, respectively. β'-In_2Se_3 is a room-temperature vdW ferroelectric material with an in-plane polarization of ~24 μCcm^{-2} along $\langle 11\bar{2}0 \rangle$ (calculated value)[48,49]. CBNO (space group of $P2_1am$, No. 26) is a quasi-vdW ferroelectric Dion-Jacobson (DJ) phase oxide[50] with a high T_C of about 1033 °C[51] and an in-plane polarization of above 40 μCcm^{-2} along the *a* axis[52,53]. ZnO is a conventional pyroelectric material with its polarization along *c* axis[54]. The unit cells of these three materials are highlighted in dashed rectangles in Fig. 2a, e and i, respectively. Here the polar axes of all three materials are parallel to the substrate surface. For pyroelectric study, we focus on the in-plane polarization[49,55-57] mainly due to that the out-of-plane polarization in 2D may suffer from the depolarization field issue[58-60] which makes the isolation of the contribution of electron-phonon renormalization difficult. To study the dimensionality effect, freestanding crystals are preferred. It is a challenge to make truly suspended devices so the sheets studied here are mechanically transferred ones free of strong substrate interactions.

We fabricate freestanding In_2Se_3, CBNO and ZnO sheets/nanomembranes with different thicknesses by mechanical exfoliation from a commercial bulk crystal (Fig. 2a,b), molten salt-assisted liquid phase epitaxy (LPE) followed by mechanical exfoliation (Fig. 2e,f), and pulsed laser deposition (PLD) followed by etching substrate away (Fig. 2i,j), respectively (see Methods). With these pyroelectric sheets at different thicknesses (8 different thicknesses from 11 nm to 222 nm for In_2Se_3, 11 thicknesses from 12 nm to 250 nm for CBNO and 7 thicknesses from 32 nm to 1920 nm for ZnO), we apply a standard periodic pulse technique to characterize the thickness-dependent pyroelectric coefficients. We use molecular dynamics (MD) simulations with a toy model to study the effects of thickness and out-of-plane bonding strength on the mean square displacement of lattice. We further investigate the temperature-dependent core/valence electron evolutions via Raman spectroscopy and DW factors via synchrotron X-ray diffraction (XRD) on pyroelectric sheets with various thicknesses. We unveil the evidence on the correlation among electron-phonon renormalization, pyroelectric response and dimensionality-tuned lattice dynamics. We show that the softening and increased vibration amplitude of optical phonons in ultrathin nanomembranes could be an important factor in enhancing the pyroelectric coefficients of pyroelectric materials.

Epitaxy growth and structural characterizations

To investigate the intrinsic in-plane pyroelectricity, single crystalline or epitaxial samples are desirable. The In_2Se_3 sheet fabricated by mechanical exfoliation can inherit the high crystallinity of the bulk crystal. Fig. 2c shows an optical microscopy image of an exfoliated sheet with an atomic force microscopy (AFM)

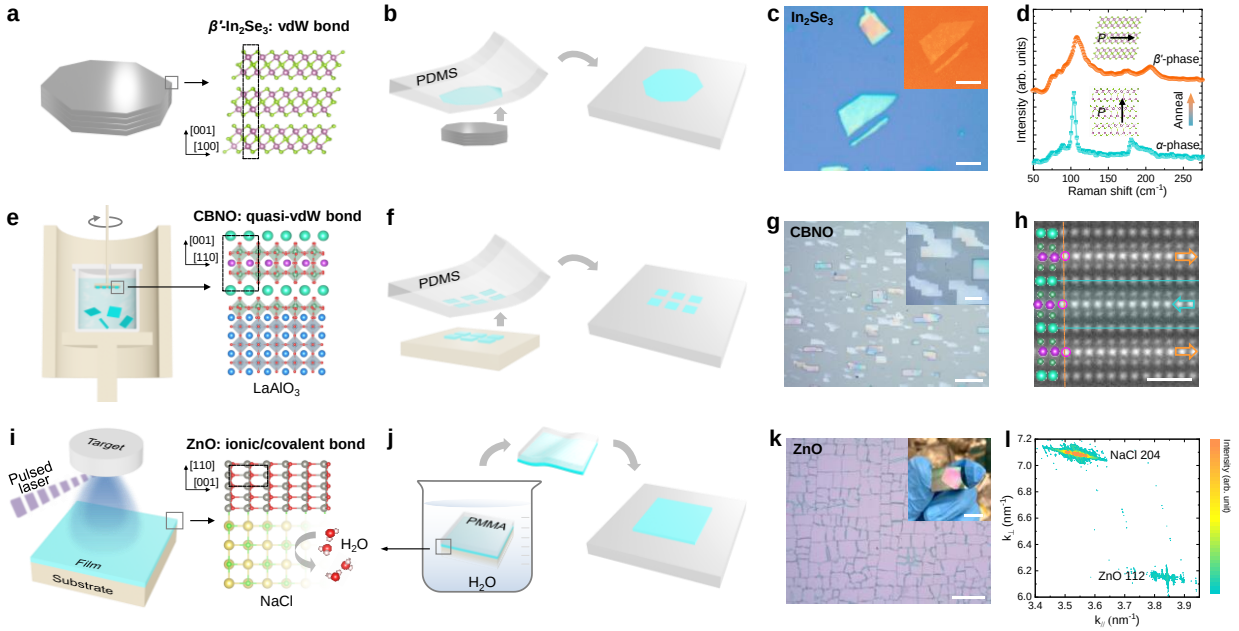

Fig. 2 | Fabrications and characterizations of sheets/nanomembranes. a, Schematic of a *β'*-In_2Se_3 bulk crystal. The atomic structure of In_2Se_3 (right panel) shows vdW bond between layers. **b**, Schematic of mechanical exfoliation (left panel) and transfer (right panel) of an In_2Se_3 sheet (cyan) by using a polydimethylsiloxane (PDMS) stamp. **c**, Optical microscopy image of an ultrathin In_2Se_3 sheet transferred on a SiO_2/Si substrate. Inset is an AFM image. The thickness of the sheet is 5-unit cells. **d**, Raman spectra of *α*-phase (cyan) and *β'*-phase (orange) In_2Se_3 at room temperature. The *β'* phase can be formed by annealing the *α* phase. Insets show the *α*-phase has out-of-plane polarization and the *β'* phase has in-plane polarization. **e**, Schematic of LPE of CBNO. The substrate is $LaAlO_3$. The cross-sectional atomic structure of CBNO (right panel) shows quasi-vdW bond along the out-of-plane direction. **f**, Schematic of mechanical exfoliation (left panel) and transfer (right panel) of CBNO sheets (cyan) by using a PDMS stamp. **g**, Optical microscopy image of epitaxial sheets on the substrate. Inset is an enlarged view. **h**, Cross-sectional STEM image of the CBNO sheet with [010] zone axis, revealing 180° domain walls (cyan lines). The atomic model of a one-unit cell for each layer is shown at the left side. Dashed orange line and dashed purple circles are guides for the eyes. Polarization directions are indicated by orange and cyan arrows pointing to the left and right, respectively. The Bi ion (purple color) away from its equivalent position represents to the polarization direction. Scale bar, 2 nm. **i**, Schematic of PLD of ZnO film. The substrate is NaCl. The cross-sectional atomic structure of ZnO (right panel) shows ionic/covalent bond. *c*-axis of ZnO is along the in-plane direction. **j**, Schematic of dissolving NaCl in water (left panel) and transfer (right panel) of a ZnO film. The film is supported by a polymethyl methacrylate (PMMA) film during the process and the PMMA is removed by acetone. **k**, Optical microscopy image of a ZnO film transferred on a SiO_2/Si substrate. Inset shows the whole centimeter-scale film. **l**, RSM of as-grown ZnO film on NaCl substrate, showing the epitaxial relationship (out-of-plane: ZnO(110)‖NaCl(001), in-plane: ZnO[001]‖NaCl[100]).

image in the inset. We use Raman spectroscopy to characterize its phase. Fig. 2d shows the Raman spectra of an as-transferred sheet after annealing (top, orange) and the sheet before annealing (bottom, cyan) for comparison. For the bottom spectrum, the peak positions at about 90 cm^{-1}, 104 cm^{-1} and 180 cm^{-1} can be assigned to E^2, A_1^1 and E^4 phonon modes, respectively, of *α*-In_2Se_3[61,62]. For the top spectrum, the peak positions at about 109 cm^{-1}, 175 cm^{-1} and 206 cm^{-1} can be attributed to the phonon modes of *β'*-In_2Se_3[62,63].

LPE provides high quality of epitaxial films or sheets and it is suitable for the preparation of complex oxides[64]. We chose $LaAlO_3$ (LAO) as substrate for the epitaxial growth of CBNO sheets due to their relatively small lattice mismatch (about 1.7% for in-plane CBNO[110]‖LAO[100] and 4.1% for in-plane CBNO[100]‖LAO[100]). The right panel of Fig. 2e shows a schematic of the cross-sectional atomic structure of CBNO/LAO. Fig. 2g shows an optical microscopy image of epitaxial CBNO sheets with an

enlarged view in the inset. The sheets distribute regularly on the LAO substrate with their main four edges parallel to those of the substrate, respectively, implying an epitaxial growth. Further, we have grown large epitaxial sheets with a side length of about 200 μm and freestanding sheets with the size up to millimeter, as shown in Supplementary Fig. 1a and b, respectively. Scanning electron microscopy (SEM) and AFM images in Supplementary Fig. 2a–c and d,e, respectively, reveal morphology of as-grown individual sheets. Due to the layered nature of CBNO, we can obtain freestanding ultrathin sheets (few layers down to monolayer) by mechanical exfoliation, as shown in Supplementary Fig. 3a–e. We have observed screw dislocations on the surface of the sheets from the AFM images in Supplementary Fig. 4a–c, revealing that LPE has a low supersaturation leading to a screw dislocation-driven growth mode[65,66] (see Supplementary Discussion 2).

We have conducted XRD and aberration-corrected STEM to characterize the crystallinity of epitaxial CBNO sheets on LAO and the epitaxial relationship, as discussed in Supplementary Discussion 3 and shown in Supplementary Fig. 5a–c. Further, we have characterized the symmetry and structure of an individual sheet by rotational anisotropy second harmonic generation (SHG), electron backscatter diffraction (EBSD) and reflection high energy electron diffraction (RHEED), as shown in Supplementary Fig. 6, 7a–e and 8a–f, respectively (see Supplementary Discussion 3). Besides, by using transmission measurement, we have estimated the band gap of CBNO, which is about 3.64 eV (see Supplementary Fig. 9 and Supplementary Discussion 4).

As a ferroelectric material, ferroelastic domains are naturally formed, which can be characterized by STEM and transmission electron microscope (TEM)[67]. The cross-sectional STEM image of a CBNO sheet (zone axis of [010]) with assigned atoms in Fig. 2h clearly reveals in-plane polarization directions pointing to the left (cyan arrow) and right (orange arrows). These directions correspond to different Bi ion displacements (dashed purple circles and a dashed orange line are guides for the eyes). We can find two kinds of domains and 180° (parallel) domain walls (horizontal cyan lines). TEM images in Supplementary Fig. 10a,b and a diffraction pattern in Supplementary Fig. 10c (zone axis of [001]) clearly show periodical domain stripes and spots splitting, respectively. The spots splitting could be originated from two domains with an in-plane rotation of 90° from each other (a-a domains)[68]. We can also observe the spot splitting in a fast Fourier transform (FFT) image (Supplementary Fig. 10e) transformed from a STEM image (zone axis of [001], Supplementary Fig. 10d). Supplementary Fig. 10f shows an inverse FFT from the FFT with white spots highlighting the lattice for one domain, resulting in one domain with a perfect atomic structure while the other domain slightly distorted. It clearly shows a 90° domain wall. The domain wall is along {110} planes, as sketched in the atomic model of Supplementary Fig. 10g. Such domain arrangements (orthogonal and parallel) help to alleviate electrostatic energy and spontaneous strains. Details of ferroelastic domains are discussed in Supplementary Discussion 5.

For ZnO, freestanding sheets cannot be fabricated by mechanical exfoliation since it is a non-vdW material. Here, we have fabricated freestanding ZnO films by using a water-soluble substrate NaCl for epitaxial growth followed by etching NaCl through water. Optical microscopy images in Supplementary Fig. 11a–d show the morphology of epitaxial films with different thicknesses. We can observe aligned wrinkles in thin films (32 nm) and cracks in thick films (160–1920 nm). These wrinkles and cracks could be originated from the large difference of thermal expansion coefficients between ZnO (1.57×10^{-5} K^{-1})[69] and NaCl (4.0×10^{-5} K^{-1})[70]. Optical microscopy images in Fig. 2k show a centimeter-scale film transferred on a SiO_2/Si substrate. We have conducted XRD measurements to study the crystallographic orientation of the film and its epitaxial relationship to the substrate. 2θ scans (changing the diffraction angle) in Supplementary Fig. 12a show that the film grows along [110] direction (out-of-plane epitaxial relation is ZnO(110)‖NaCl(001)). The reciprocal space mapping (RSM) in Fig. 2l and φ scans (rotating the sample around its normal direction at a fixed diffraction angle) in Supplementary Fig. 12b,c reveal that the in-plane epitaxial relationship is ZnO[001]‖NaCl[100] (note that two equivalent perpendicular domains exist and the lattice mismatch between ZnO(002) and NaCl(100) is 5.6%) and this epitaxial film (160 nm) is fully relaxed. 2θ scans in Supplementary Fig. 12d confirm the same out-of-plane reflection (110) in the transferred film as the as-grown one.

Dimensionality effect on pyroelectricity

To measure the pyroelectric coefficients in micrometer-scale sheets with different thicknesses, we use a periodic pulse technique (or Chynoweth technique[71]). Supplementary Fig. 13 shows a schematic of the pyroelectric measurement. Basically, the optical path of a high-power CW infrared (IR) laser is spatially modulated by an external optical chopper. By programming the frequency of the chopper, the laser illumination is periodically blocked and allowed to hit the surface of the pyroelectric device yielding periodic cooling and heating with controlled duration on the device. With lock-in amplification, such setup results in measurable pyroelectric currents even in the micrometer-scale sheet. To evaluate the temperature, we track the change of the resistance of a thin Ni stripe (~20 nm) under laser heating. Through the temperature coefficient of its resistance, we can calibrate the temperature change at the substrate surface, as shown in Supplementary Fig. 14 (circuit diagram) and 15a–d (measurements) (see Supplementary Discussion 6).

Fig. 3a shows a schematic illustration of the pyroelectric device. We have fabricated sheet-based pyroelectric devices by using a dry transfer technique (see Methods) with few-layer graphene (FLG) as electrode instead of depositing metal layer to reduce the possible clamping effect from the substrate. Fig. 3b, c and d show optical microscopy images of representative devices for In_2Se_3, CBNO and ZnO, respectively (bottom panels), and their cross-sectional atomic models (top panels). It is observed that right after the IR laser illumination is switched from the "ON" state to "OFF" state or from "OFF" to "ON", (when the illumination hits the surface of the device through the gap of the chopper blades, it is the "ON" state; when the illumination is blocked by the chopper blade, it is the "OFF" state), the pyroelectric current (and current density) ramps rapidly to a maximum absolute value and then decays in a relatively slow rate, as shown in Fig. 3e, f and g for devices in Fig. 3b, c and d, respectively. Such result is consistent with the common observations in pyroelectric tests by the periodic pulse technique: the transition between "ON" and "OFF" state induces a large temperature fluctuation (thus large pyroelectric current) due to a sudden presence or removal of heat source; within consistent heating or cooling states, temperature fluctuation becomes less dramatic leading to smaller pyroelectric response. The effective electrode area in this study is estimated by the electrode length (measured by optical microscopy, e.g., Supplementary Fig. 16–18a) multiplied by the sheet thickness (measured by AFM, e.g., Supplementary Fig. 16–18b,c). To improve statistics, we have fabricated and measured more devices (26 in total) with different thicknesses, as shown in Supplementary Fig. 19–25 for In_2Se_3-based, Supplementary Fig. 26–35 for CBNO-based and Supplementary Fig. 36–40 for ZnO-based. For ferroelectric materials, the direction of pyroelectric current can be switched by flipping the polarization. Indeed, we can observe the switchable pyroelectric currents after switching polarizations (positive to negative) in In_2Se_3-based devices (Fig. 3e and Supplementary Fig. 19, 21, 24) and CBNO-based devices (Supplementary Fig. 27, 29, 35). This switchablity can rule out other possible charging scenarios such as thermoelectric effect.

Assuming a constant pyroelectric coefficient p within a certain range of temperatures during measurements, p can be expressed by:

$$p = \frac{J\Delta t}{\Delta T} = \frac{\sigma}{\Delta T}, \quad (3)$$

where J is the measured current density, σ is the charge density obtained by integrating J with respect to t, ΔT is the temperature change. In the current density versus time curve, usually the part corresponding to heating is chosen for extracting pyroelectric coefficients[72]. Accordingly, we have calculated pyroelectric coefficients (absolute effective values) for all devices and plotted them as a function of the sheet thickness in Fig. 3h, i and j for In_2Se_3, CBNO and ZnO, respectively. These plots clearly show a remarkable thickness dependence of the pyroelectric coefficient in all three materials. Specifically, for In_2Se_3, the pyroelectric coefficient increases from 958.8 $\mu Cm^{-2}K^{-1}$ at a thickness of 222 nm to 5.5×10^3 $\mu Cm^{-2}K^{-1}$ at 11 nm; for CBNO, it increases from 2.0 $\mu Cm^{-2}K^{-1}$ at a thickness of 250 nm to 110.8 $\mu Cm^{-2}K^{-1}$ at 12 nm; and for ZnO, it increases from 42 $\mu Cm^{-2}K^{-1}$ at a thickness of 1920 nm to 8.7×10^3 $\mu Cm^{-2}K^{-1}$ at 32 nm. We find that the ratios of pyroelectric coefficients between thinnest and thickest films studied here are 6 for In_2Se_3, 55 for CBNO and 207 for ZnO. ZnO exhibits the strongest dimensionality effect and In_2Se_3 weakest.

The figure of merit (F_V) of a pyroelectric material is often defined as: $F_V = p/c_p\varepsilon_r\varepsilon_0$, where c_p is the specific heat capacity, ε_0 is the permittivity of free space and ε_r is the relative permittivity of the pyroelectric

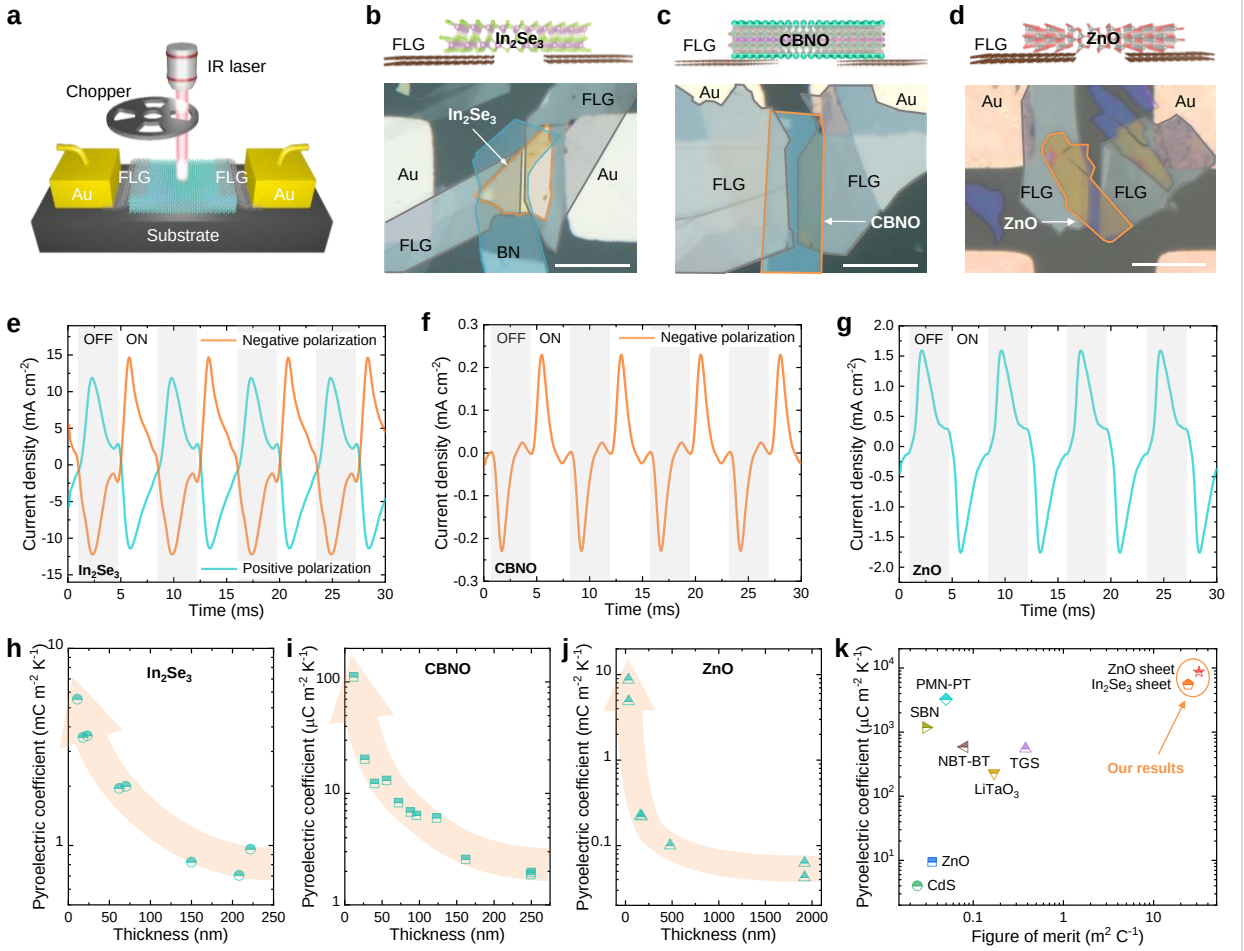

Fig. 3 | Pyroelectricity in In_2Se_3, CBNO and ZnO and the dimensionality effect. a, Schematic of the pyroelectric device model. Chopper is used to modulate the IR laser. **b**,**c**,**d**, Optical microscopy images of representative devices for In_2Se_3 (**b**), CBNO (**c**) and ZnO (**d**) (bottom panels) and their cross-sectional atomic structures (top panels). **e**,**f**,**g**, Pyroelectric current density under the modulated IR laser for the In_2Se_3-based device in **b** (**e**), CBNO-based device in **c** (**f**) and ZnO-based device in **d** (**g**). Orange curves in **e** and **f** are measured after positive poling and the cyan curve in **e** is measured after negative poling. **h**,**i**,**j**, Effective pyroelectric coefficients as a function of sheet thickness for In_2Se_3 (**h**), CBNO (**i**) and ZnO (**j**). Light orange arrows are guides for the eyes. **k**, Comparison of the pyroelectric coefficients and the figures of merit of In_2Se_3 (11 nm) and ZnO (32 nm) with those of conventional single-crystalline and epitaxial pyroelectric materials including ZnO[55], GaN[78], CdS[79], triglycine sulfate (TGS)[79], $LiTaO_3$[6], $LiNbO_3$[80], $PbTiO_3$[81], $0.79Pb(Mg_{1/3}Nb_{2/3})O_3$-$0.21PbTiO_3$ (PMN-PT)[82], Mn:$0.946Na_{0.5}Bi_{0.5}TiO_3$-$0.054BaTiO_3$ (NBT-BT)[83], $Sr_{0.5}Ba_{0.5}Nb_2O_6$ (SBN)[84]. The value for GaN is measured at 160 ˚C, for TGS is at 50 ˚C, for PMN-PT is at 55 ˚C, values for In_2Se_3 and ZnO here are measured in the range of 50–170 ˚C and for others are at room temperature.

material[6]. The c_p and ε_r for In_2Se_3 are 1.5 $JK^{-1}cm^{-3}$ and 17, respectively[73,74], and for ZnO are 2.9 $JK^{-1}cm^{-3}$ and 10.4, respectively[75,76] (c_p for CBNO has not been reported). Thus, we obtain F_V of 24.2 m^2C^{-1} for the In_2Se_3 sheet with the thickness of 11 nm and 32.6 m^2C^{-1} for the ZnO sheet with the thickness of 32 nm. Fig. 3k summarizes the pyroelectric coefficients and figures of merit for In_2Se_3 (11 nm) and ZnO (32 nm) sheets as well as most single crystalline and epitaxial pyroelectric materials including ZnO[54], GaN[77], CdS[78], triglycine sulfate (TGS)[79], $LiTaO_3$[6], $LiNbO_3$[80], $PbTiO_3$[81], $0.79Pb(Mg_{1/3}Nb_{2/3})O_3$-$0.21PbTiO_3$ (PMN-PT)[82], Mn:$0.946Na_{0.5}Bi_{0.5}TiO_3$-$0.054BaTiO_3$ (NBT-BT)[83] and $Sr_{0.5}Ba_{0.5}Nb_2O_6$ (SBN)[84]. Here, single crystals or epitaxial films are mainly presented since we only focus on intrinsic pyroelectric property (polycrystalline ceramics materials or engineered interface structures (e.g., Au/Nb:$Ba_{0.6}Sr_{0.4}TiO_3$[47]) are complexed by some

extrinsic mechanisms such as grain-size effects[85] and Schottky junctions[47]). The experimentally demonstrated pyroelectric coefficients for In_2Se_3 (11 nm) and ZnO (32 nm) are one to a few orders of magnitude higher than most conventional pyroelectric crystals and slightly larger than PMN-PT. Moreover, the figures of merit for In_2Se_3 (11 nm) and ZnO (32 nm) are more than one order of magnitude larger than these conventional pyroelectric crystals.

Crystal lattice dynamics

Pyroelectric coefficient is directly related to lattice dynamics in pyroelectric crystals, as described in Eq. (2). To understand the effects of out-of-plane bonding strength and sheet thickness on lattice dynamics, with a hexagonal closed-packed (HCP) solid as a toy model, we have carried out a series of MD simulations (see Methods). We focus on the relation between mean square displacement $\langle {u_l}^2 \rangle$ and out-of-plane bonding strength/sheet thickness. The use of the HCP model rather than the real materials allows us to be able to simulate a sheet with large enough lateral size which is needed for the observation of substantial dimensionality effect on phonon dynamics[27]. Supplementary Videos 1–6 show the animations of the simulated results with the lattice vibrations of the sheet tuned by varied thickness and out-of-plane bonding strength. Fig. 4a shows the $\langle {u_l}^2 \rangle$ alone in-plane directions as a function of step time in sheets of 32 layers (left), 16 layers (middle) and 10 layers (right). As the thickness decreases, the in-plane $\langle {u_l}^2 \rangle$ increases for both out-of-plane bonding strengths of ε_e and $\varepsilon_e/2$. In Fig. 4b, we have plotted the average in-plane $\langle {u_l}^2 \rangle$ in all three types of sheets as a function of the thickness and out-of-plane bonding strength. In Fig. 4c, their percentage changes versus thickness are plotted. For the case of out-of-plane bonding strength ε_e, the in-plane $\langle {u_l}^2 \rangle$ for 10-layer sheet shows an enhancement of (8.7±1.9)% compared with 32 layers, while for the case of $\varepsilon_e/2$, it shows an enhancement of (3.9±1.3)%. These

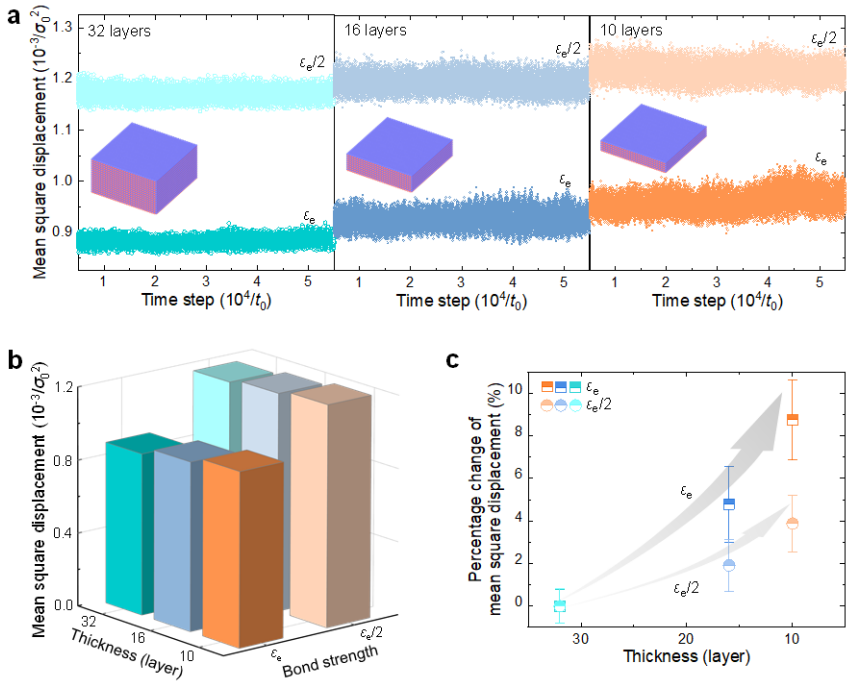

Fig. 4 | MD simulations in model hexagonal closed packed sheets. a, Mean square displacement $\langle {u_l}^2 \rangle$ along in-plane directions as a function of time step in model sheets with out-of-plane bonding strengths of ε_e and $\varepsilon_e/2$ and thicknesses of 32 layers (left), 16 layers (middle) and 10 layers (right). Insets are the corresponding model sheets. ε_e, σ_0 and t_0 are the energy, length and time units, respectively (see Methods). **b**, Average $\langle {u_l}^2 \rangle$ as a function of out-of-plane bonding strength and thickness. **c**, Percentage change of average $\langle {u_l}^2 \rangle$ as a function of thickness. The sheet with stronger out-of-plane bonding strength has more pronounced dimensionality effect on $\langle {u_l}^2 \rangle$. Gray arrows are guides for the eyes.

simulation results clearly reveal the dimensionality effect on mean square displacement which is more pronounced in sheets with stronger out-of-plane bonding strength. The total $\langle {u_l}^2 \rangle$ also shows a similar phenomenon (Supplementary Fig. 41a–c). It is noted that further reducing the out-of-plane bonding strength or thickness within this model system could significantly affect its structural stability.

Despite the use of computationally large supercells in our MD simulations, the MD supercells only qualitatively characterize the dimensionality effect. This is because experimentally accessible samples are much larger in size and more complex in chemistry. Thus, experimental investigations are needed to understand the thickness- and bonding strength-dependent lattice dynamics. The phonon dynamics in classical ferroelectric perovskites have been widely investigated by Raman spectroscopy[86]. Hence, we have conducted Raman measurements on freestanding In_2Se_3, CBNO and ZnO sheets. Supplementary Fig. 42a–f and 43a–j show optical microscopy and AFM images, and temperature-dependent Raman spectra for In_2Se_3 and CBNO sheets, respectively. Supplementary Fig. 44a,b show an optical microscopy image and Raman spectra for ZnO sheets (temperature-dependent measurements is not performed on ZnO sheets due to the low Raman signal). To investigate the dimensionality effect, we have measured two types of samples (thick and thin) for comparison for each material. The thicknesses of thick and thin sheets are 280 nm and 29 nm for In_2Se_3, respectively, and 730 nm and 35 nm for CBNO, respectively. Here, we focus on the phonon with a frequency of ~109 cm^{-1} for In_2Se_3 and phonon with a frequency of ~585 cm^{-1} for CBNO, as shown in Fig. 5a and b, respectively. The phonon at ~109 cm^{-1} for In_2Se_3 could be assigned to the A_g^2 mode[61] and the phonon at ~585 cm^{-1} for CBNO could be attributed to a small distortion of NbO_6 octahedra along the in-plane direction (in-plane phonon, as schematically illustrated in the inset of Fig. 5f)[87].

Fig. 5c and f plot peak positions of the A_g^2 phonon of In_2Se_3 and in-plane phonon of CBNO, respectively, at different temperatures. Both phonons show a decreasing frequency with increasing temperature in both thick and thin sheets. The temperature-dependent shift of the phonon frequency mainly originates from the thermal expansion of the lattice and phonon-phonon interactions[88,89]. The phonon frequency at temperature T above room temperature (293 K) can be written by the first-order approximation as[88-90]:

$$\omega(T) = \omega_0 + \Delta\omega_e(T) + \Delta\omega_d(T) \approx \omega(293) + k_e(T - 293) + k_d(T - 293), \quad (4)$$

where ω_0 is the frequency of phonon mode in a perfect harmonic lattice, $\Delta\omega_e(T)$ represents the frequency shift due to the thermal expansion of lattice[91], $\Delta\omega_d(T)$ represents the frequency shift due to the phonon decay into phonons with lower energy[89], and k_e and k_d are the linear slope of the first-order approximation of the thermal expansion and phonon decay contributions, respectively. The detailed discussion of $\Delta\omega_e(T)$ and $\Delta\omega_d(T)$ is presented in Supplementary Discussion 7. The experimental temperature-dependent frequencies of both phonons (In_2Se_3 and CBNO) for both thick and thin sheets can be linearly fitted by the first-order approximation Eq. (4), yielding $k_e + k_d$ of –(7.64±0.98)×10^{-3} $cm^{-1}K^{-1}$ and –(1.79±0.21)×10^{-2} $cm^{-1}K^{-1}$ for the A_g^2 phonon in the thick and thin In_2Se_3 sheets, respectively, and –(1.22±0.12)×10^{-2} $cm^{-1}K^{-1}$ and –(3.17±0.26)×10^{-2} $cm^{-1}K^{-1}$ for the in-plane phonon in the thick and thin CBNO sheets, respectively. For In_2Se_3, the thin sheet shows a larger slope (enhancement of 134.3%) of the A_g^2 phonon shift than the thick one. For CBNO, the thin sheet shows a larger slope (enhancement of 159.8%) of the in-plane phonon shift than the thick one. The larger slope of phonon shift in the thin sheet compared with the thick one suggests that the thin sheet has a more significant temperature dependence, thus possibly a more pronounced pyroelectric response.

Fig. 5d and g show the full-width-at-half-maximums (FWHMs) of the A_g^2 phonon of In_2Se_3 and the in-plane phonon of CBNO, respectively. Both phonons show an increasing FWHM values with increasing temperature in both thick and thin sheets. Usually, the phonon damping is likely caused by the phonon confinement, defect scattering and residual stress[92]. Here, since both In_2Se_3 and CBNO samples are single crystals with low defects, the observed phonon damping may mainly originate from the phonon-phonon interactions[88,89]. By the first-order approximation (linear fitting), slopes of (3.54±0.27)×10^{-2} $cm^{-1}K^{-1}$ and (5.92±0.22)×10^{-2} $cm^{-1}K^{-1}$ are obtained for the A_g^2 phonon in the thick and thin In_2Se_3 sheets, respectively, and slopes of (1.58±0.17)×10^{-2} $cm^{-1}K^{-1}$ and (4.35±0.48)×10^{-2} $cm^{-1}K^{-1}$ are obtained for the in-plane phonon

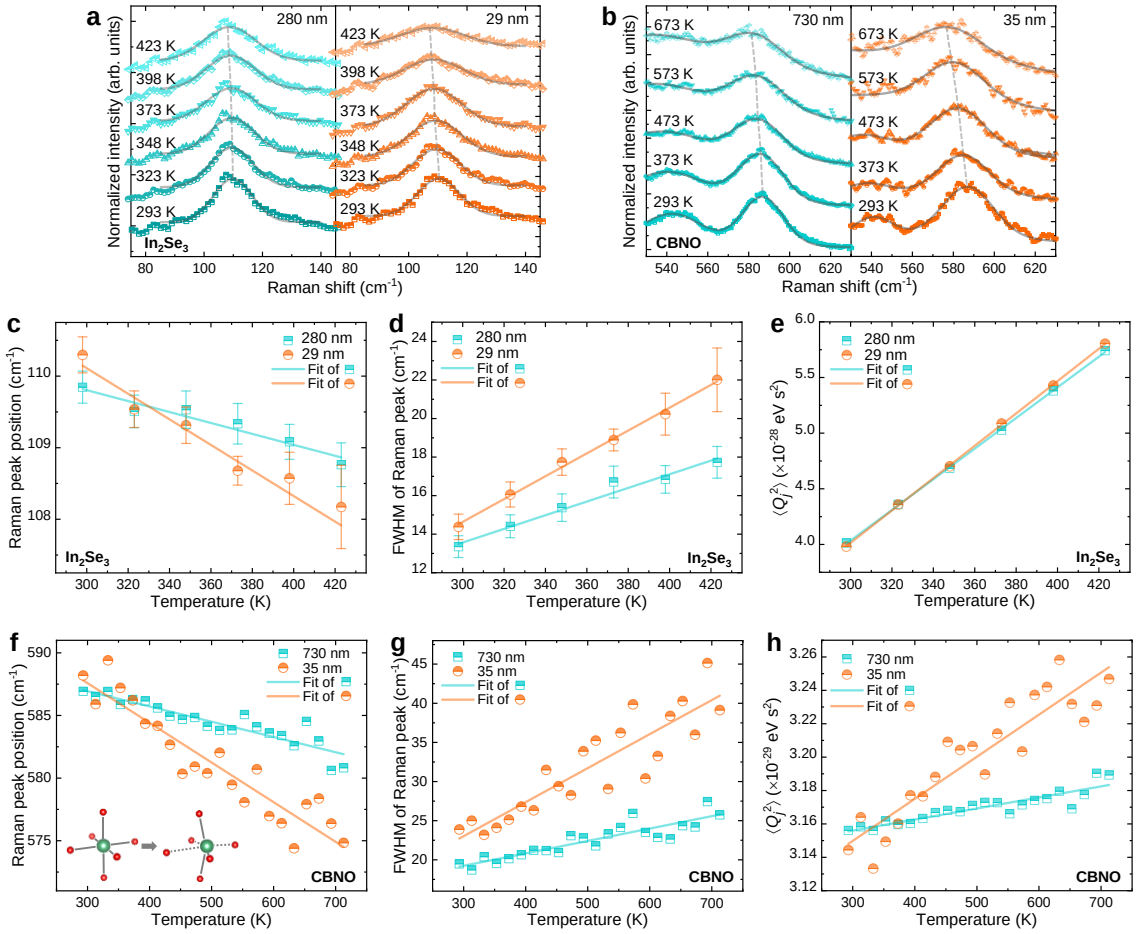

Fig. 5 | Crystal lattice dynamics in In_2Se_3 and CBNO. a, Temperature-dependent (from 293 to 423 K) Raman spectra at ~109 cm^{-1} (A_g^2 mode) in a thick In_2Se_3 sheet (280 nm, left panel) and a thin In_2Se_3 sheet (29 nm, right panel). **b**, Temperature-dependent (from 293 to 673 K) Raman spectra at ~587 cm^{-1} (in-plane mode) in a thick CBNO sheet (730 nm, left panel) and a thin CBNO sheet (35 nm, right panel). Dashed lines are guides for the eyes. **c**,**d**,**e**, Peak position (**c**), FWHM (**d**) and mean square amplitude $\langle Q_j^2 \rangle$ (**e**) of the A_g^2 phonon of In_2Se_3 as a function of temperature in the thick sheet (half-filled squares in cyan) and thin sheet (half-filled circles in orange). **f**,**g**,**h**, Peak position (**f**), FWHM (**g**) and mean square amplitude $\langle Q_j^2 \rangle$ (**h**) of the in-plane phonon of CBNO as a function of temperature in the thick sheet (half-filled squares in cyan) and thin sheet (half-filled circles in orange). The inset of **f** is a schematic of the in-plane mode of CBNO. Cyan and orange lines are linear fittings.

in the thick and thin CBNO sheets, respectively. For both In_2Se_3 and CBNO, the thin sheet shows a larger slope of phonon damping compared with the thick one, indicating a significant contribution from phonon-phonon interactions. The slope enhancement for the thin sheet compared with the thick one for CBNO is 175.3%. The slope enhancement for In_2Se_3 is 67.2%. This observation implies that the large slope enhancement ($k_e + k_d$) for the phonon frequency in Fig. 5c,f is largely responsible by phonon-phonon interactions (k_d). It is noted that the enhancements of phonon softening and damping for the ~933 cm^{-1} phonon in the thin CBNO sheet compared with the thick one are less significant, as shown in Supplementary Fig. 45a–d and discussed in Supplementary Discussion 7.

According to Eq. (2), the second-order primary pyroelectricity $p_1^{(2)}$ is directly related to the mean square amplitude of normal modes and its temperature derivative $d\langle Q_j{}^2\rangle/dT$. Here, $\langle Q_j{}^2\rangle$ can be expressed by[4]

$\langle {Q_j}^2 \rangle = \frac{\hbar}{2}\frac{2n_j+1}{\omega_j}$, (5)

where ω_j is the phonon eigenfrequency and n_j is the Bose-Einstein distribution function. Here, for simple estimations, we use the measured phonon frequency to represent ω_j. Fig. 5e and h plot $\langle {Q_j}^2 \rangle$ of the A_g^2 phonon of In_2Se_3 and the in-plane phonon of CBNO, respectively, as a function of temperature for both thick and thin sheets. Linear fittings yield slope enhancements of 5.1% (from 1.38×10^{-30} eVs^2K^{-1} to 1.45×10^{-30} eVs^2K^{-1}) for the A_g^2 phonon of In_2Se_3 and 280% (from 6.62×10^{-34} eVs^2K^{-1} to 25.20×10^{-34} eVs^2K^{-1}) for the in-plane phonon of CBNO for the thin sheet compared with the thick one.

It is technically difficult to use Raman measurements to access all $\langle {Q_j}^2 \rangle$ and not all modes contribute significantly to the pyroelectric behavior. Also, in our analysis, to reduce experimental artifacts, we only focus on the modes with reasonable signal-to-noise ratio. Although only limited number of phonon mode for each material is analyzed (its $d\langle {Q_j}^2 \rangle/dT$ partially contributes to ${p_1}^{(2)}$), our measured pyroelectric coefficients (Fig. 3h,i) for the similar thicknesses have the same trends with these phonon dynamic behaviors, especially for CBNO (~5 times enhancement of pyroelectric coefficients between 40 nm and 250 nm versus ~2.8 times enhancement of $d\langle {Q_j}^2 \rangle/dT$ of the in-plane phonon between 35 nm and 735 nm). The small enhancement for In_2Se_3 suggests that the contribution of the A_g^2 phonon to its pyroelectricity is minor. It is possible that some phonons may have more pronounced contributions. However, their signal-to-noise ratios are too small to conduct reliable analysis. Nevertheless, these results clearly show that the DW second order effect associated with electron-phonon renormalization plays a conclusive role on the dimensionality effect for pyroelectricity.

Another experimental approach to evaluate the dimensionality effect is to directly probe the DW factor of sheets of different thicknesses. The DW factor can be experimentally determined from the Bragg peak intensity measured by XRD. The intensity of a Bragg peak as a function of temperature is expressed as[93]:

$I = I_0 e^{-G^2\langle {u_l}^2 \rangle}$, (6)

where $e^{-G^2\langle {u_l}^2 \rangle}$ is the DW factor and $G = 2\pi/d$ is the reciprocal lattice vector (d is the interplanar spacing). The mean square displacement $\langle {u_l}^2 \rangle$ is related to $\langle {Q_j}^2 \rangle$ through $\langle u_l \rangle = \sum_j \langle Q_j \rangle \epsilon_j / \sqrt{M_l}$, where ϵ_j is the normalized Cartesian component of the eigenvector of the usual (mass-weighted) harmonic dynamical matrix and M_l is the atomic mass[94]. Thus, a stronger temperature dependence of DW factor (or $\langle {u_l}^2 \rangle$) reflects a larger $d\langle {Q_j}^2 \rangle/dT$. To study the dimensionality effect on pyroelectricity (here ${p_1}^{(2)}$ is focused), we can measure the DW factors for sheets with different thicknesses and analyze their temperature dependences.

In this study, we use a synchrotron X-ray source to characterize the DW factors. Fig. 6a shows a schematic of the synchrotron XRD measurement. Here we use CBNO as the model system since it has reasonable chemical and phase stability at reduced dimension at a large temperature window under high-flux X-ray beam. We have performed 2θ scans and φ scans on four CBNO sheets (samples S1, S2, S3 and S4 shown in optical microscopy images in Supplementary Fig. 46a, d, g and l, respectively) with different thicknesses (410 nm, 268 nm, 98 nm and 53 nm shown in AFM images in Supplementary Fig. 46b,c, e,f, h,i and m,n, respectively) from room temperature to 800 °C. Fig. 6b and c show temperature-dependent 006 reflections for S1 (410 nm) and S4 (53 nm), respectively. Fig. 6d and e show temperature-dependent 026 reflections for S1 and S4, respectively. 006 and 206 reflections for other two samples S2 and S3 are shown in Supplementary Fig. 47a,b and c,d, respectively. 206 reflections for S1, S2 and S3 are shown in Supplementary Fig. 47e, f and g, respectively (for S4, the signal-to-noise ratio is too low to conduct conclusive analysis). We have integrated all peak intensities (in natural logarithm), as shown in Fig. 6f, g and h for 006, 026 and 206, respectively. These results show roughly linear temperature dependences. Their linear fittings yield values of $\Delta\langle {u_l}^2 \rangle/\Delta T$ for all three reflections in four samples, as plotted in Fig. 6i. It clearly shows a remarkable enhancement of $\Delta\langle {u_l}^2 \rangle/\Delta T$ for S4 (53 nm) compared with S3 (98 nm), which directly reflects an enhancement of $d\langle {Q_j}^2 \rangle/dT$ thereby a larger ${p_1}^{(2)}$. This enhancement of $\Delta\langle {u_l}^2 \rangle/\Delta T$ (~1.4 times for 026 and ~2.1 times for 006 for S4 compared with S3) is close to the

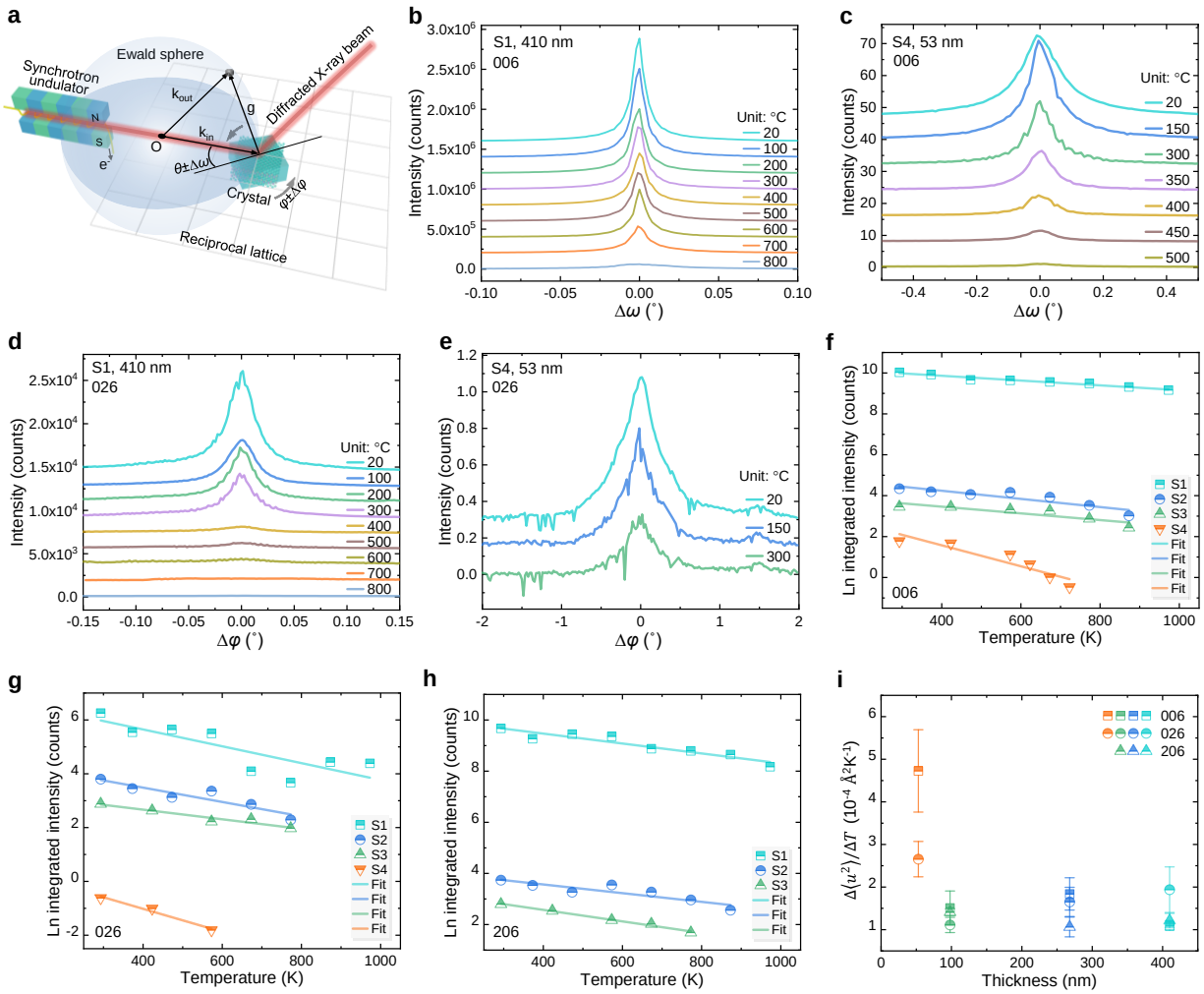

Fig. 6 | DW factor in CBNO. a, Schematic of the synchrotron XRD measurement (2θ scan and φ scan). **b**,**c**, Temperature-dependent 2θ scans of 006 reflections for CBNO sheets S1 (410 nm) (**b**) and S4 (53 nm) (**c**). **d**,**e**, Temperature-dependent φ scans of 026 reflections for sheets S1 (**d**) and S4 (**e**). Here, we need to mention that the diffraction peak position for the micrometer-scale sheet is sensitive to the alignment at different temperatures. For better illustration, we normalize all peaks with respect to the peak position and present $\Delta\omega$ and $\Delta\varphi$ instead of 2θ and φ. **f**,**g**,**h**, Temperature-dependent integrated intensities (in natural logarithm) of 006 (**f**), 026 (**g**) and 206 (**h**) reflections for all sheets. Color lines are fittings. **i**, $\Delta\langle u_l^2\rangle/\Delta T$ for reflections 006, 026 and 206 as a function of sheet thickness.

enhancement (~2 times) of our measured pyroelectric coefficients for the sheets with similar thicknesses (Fig. 3i), indicating a pronounced contribution of electron-phonon renormalization.

Conclusion

We have investigated the dimensionality effect on pyroelectricity in three types of materials (a vdW material In_2Se_3, a quasi-vdW CBNO and an ionic/covalent ZnO). We observe a universal large enhancement of pyroelectric coefficient in the thin sheet over thick one. Among three materials, ZnO shows the greatest enhancement of more than two orders of magnitude. Our measured pyroelectric coefficients and figures of merit in In_2Se_3 sheet of 11 nm and ZnO sheet of 32 nm are highest among all conventional single crystalline and epitaxial pyroelectrics. The thickness-dependent lattice dynamics revealed by MD simulations, temperature-dependent Raman spectroscopy and synchrotron XRD evidences the correlation between the electron-phonon renormalization and pyroelectricity. The discovery

opens a window on using dimensionality-controlled electron-phonon interactions to design and develop high-performance sensing and energy conversion devices.

Reference

1. Giustino, F., Louie, S. G. & Cohen, M. L. Electron-phonon renormalization of the direct band gap of diamond. *Phys. Rev. Lett.* **105**, 265501 (2010).
2. Born, M. On the quantum theory of pyroelectricity. *Rev. Mod. Phys.* **17**, 245-251 (1945).
3. Szigeti, B. Temperature dependence of pyroelectricity. *Phys. Rev. Lett.* **35**, 1532-1534 (1975).
4. Liu, J. & Pantelides, S. T. Mechanisms of pyroelectricity in three- and two-dimensional materials. *Phys. Rev. Lett.* **120**, 207602 (2018).
5. Rogers, J. A., Lagally, M. G. & Nuzzo, R. G. Synthesis, assembly and applications of semiconductor nanomembranes. *Nature* **477**, 45 (2011).
6. Whatmore, R. W. Pyroelectric devices and materials. *Rep. Prog. Phys.* **49**, 1335-1386 (1986).
7. Lang, S. B. Pyroelectricity: from ancient curiosity to modern imaging tool. *Phys. Today* **58**, 31 (2005).
8. Yang, Y., Wang, S., Zhang, Y. & Wang, Z. L. Pyroelectric nanogenerators for driving wireless sensors. *Nano Lett.* **12**, 6408-6413 (2012).
9. Wang, Z. *et al.* Light-induced pyroelectric effect as an effective approach for ultrafast ultraviolet nanosensing. *Nat. Commun.* **6**, 8401 (2015).
10. Thakre, A., Kumar, A., Song, H.-C., Jeong, D.-Y. & Ryu, J. Pyroelectric energy conversion and its applications—flexible energy harvesters and sensors. *Sensors* **19**, 2170 (2019).
11. Yang, Y. *et al.* Pyroelectric nanogenerators for harvesting thermoelectric energy. *Nano Lett.* **12**, 2833-2838 (2012).
12. Bowen, C. R. *et al.* Pyroelectric materials and devices for energy harvesting applications. *Energy Environ. Sci.* **7**, 3836-3856 (2014).
13. Pandya, S. *et al.* Pyroelectric energy conversion with large energy and power density in relaxor ferroelectric thin films. *Nat. Mater.* **17**, 432-438 (2018).
14. Sebald, G., Lefeuvre, E. & Guyomar, D. Pyroelectric energy conversion: Optimization principles. *IEEE Trans. Ultrason. Ferroelectr. Freq. Control* **55**, 538-551 (2008).
15. Belitz, R. *et al.* Waste heat energy harvesting by use of $BaTiO_3$ for pyroelectric hydrogen generation. *Energy Harvest. Syst* **4**, 107-113 (2017).
16. Xie, M., Dunn, S., Boulbar, E. L. & Bowen, C. R. Pyroelectric energy harvesting for water splitting. *Int. J. Hydrogen Energy* **42**, 23437-23445 (2017).
17. You, H. *et al.* Room-temperature pyro-catalytic hydrogen generation of 2D few-layer black phosphorene under cold-hot alternation. *Nat. Commun.* **9**, 2889 (2018).
18. Naranjo, B., Gimzewski, J. K. & Putterman, S. Observation of nuclear fusion driven by a pyroelectric crystal. *Nature* **434**, 1115-1117 (2005).
19. Geuther, J. A. & Danon, Y. Electron and positive ion acceleration with pyroelectric crystals. *J. Appl. Phys.* **97**, 074109 (2005).
20. Stewart, J. W., Vella, J. H., Li, W., Fan, S. & Mikkelsen, M. H. Ultrafast pyroelectric photodetection with on-chip spectral filters. *Nat. Mater.* **19**, 158–162 (2020).
21. Resta, R. & Vanderbilt, D. *Theory of polarization: a modern approach*. In *Physics of Ferroelectrics: A Modern Perspective* 31-68 (Springer Berlin Heidelberg, 2007).
22. Allen, P. B. & Heine, V. Theory of the temperature dependence of electronic band structures. *J. Phys. C: Solid State Phys.* **9**, 2305-2312 (1976).
23. Yan, W. S. *et al.* Temperature dependence of the pyroelectric coefficient and the spontaneous polarization of AlN. *Appl. Phys. Lett.* **90**, 212102 (2007).
24. Liu, J. & Pantelides, S. T. Pyroelectric response and temperature-induced α-β phase transitions in α-In_2Se_3 and other α-III_2VI_3 (III = Al, Ga, In; VI = S, Se) monolayers. *2D Materials* **6**, 025001 (2019).
25. Peierls, R. E. *Quantum Theory of Solids*. 108 (Oxford University Press, 1955).
26. Landau, L. The theory of phase transitions. *Nature* **138**, 840-841 (1936).
27. Mermin, N. D. Crystalline order in two dimensions. *Phys. Rev.* **176**, 250-254 (1968).

28. Mermin, N. D. & Wagner, H. Absence of ferromagnetism or antiferromagnetism in one- or two-dimensional isotropic Heisenberg models. *Phys. Rev. Lett.* **17**, 1133-1136 (1966).
29. Halperin, B. I. On the Hohenberg–Mermin–Wagner theorem and its limitations. *J. Stat. Phys.* **175**, 521-529 (2019).
30. Hohenberg, P. C. Existence of long-range order in one and two dimensions. *Phys. Rev.* **158**, 383-386 (1967).
31. Young, A. P. Melting and the vector Coulomb gas in two dimensions. *Phys. Rev. B* **19**, 1855-1866 (1979).
32. Nelson, D. R. & Halperin, B. I. Dislocation-mediated melting in two dimensions. *Phys. Rev. B* **19**, 2457-2484 (1979).
33. Kosterlitz, J. M. & Thouless, D. J. Ordering, metastability and phase transitions in two-dimensional systems. *J. Phys. C: Solid State Phys.* **6**, 1181-1203 (1973).
34. Hong, S. S. *et al.* Two-dimensional limit of crystalline order in perovskite membrane films. *Sci. Adv.* **3**, eaao5173 (2017).
35. Geim, A. K. & Novoselov, K. S. The rise of graphene. *Nat. Mater.* **6**, 183 (2007).
36. Yu, Y. *et al.* High-temperature superconductivity in monolayer $Bi_2Sr_2CaCu_2O_{8+\delta}$. *Nature* **575**, 156–163 (2019).
37. Ji, D. *et al.* Freestanding crystalline oxide perovskites down to the monolayer limit. *Nature* **570**, 87-90 (2019).
38. Huang, B. *et al.* Layer-dependent ferromagnetism in a van der Waals crystal down to the monolayer limit. *Nature* **546**, 270-273 (2017).
39. Gong, C. *et al.* Discovery of intrinsic ferromagnetism in two-dimensional van der Waals crystals. *Nature* **546**, 265 (2017).
40. Fei, Z. *et al.* Two-dimensional itinerant ferromagnetism in atomically thin Fe_3GeTe_2. *Nat. Mater.* **17**, 778-782 (2018).
41. Yoshida, M., Suzuki, R., Zhang, Y., Nakano, M. & Iwasa, Y. Memristive phase switching in two-dimensional 1T-TaS_2 crystals. *Sci. Adv.* **1**, e1500606 (2015).
42. Xi, X. *et al.* Strongly enhanced charge-density-wave order in monolayer $NbSe_2$. *Nat. Nanotechnol.* **10**, 765 (2015).
43. Jiang, D. *et al.* High-Tc superconductivity in ultrathin $Bi_2Sr_2CaCu_2O_{8+x}$ down to half-unit-cell thickness by protection with graphene. *Nat. Commun.* **5**, 5708 (2014).
44. Tusche, C., Meyerheim, H. L. & Kirschner, J. Observation of depolarized ZnO(0001) monolayers: Formation of unreconstructed planar sheets. *Phys. Rev. Lett.* **99**, 026102 (2007).
45. Xue, F. *et al.* Room-temperature ferroelectricity in hexagonally layered α-In_2Se_3 nanoflakes down to the monolayer limit. *Adv. Funct. Mater.* **28**, 1803738 (2018).
46. Meirzadeh, E. *et al.* Surface pyroelectricity in cubic $SrTiO_3$. *Adv. Mater.* **31**, 1904733 (2019).
47. Yang, M.-M. *et al.* Piezoelectric and pyroelectric effects induced by interface polar symmetry. *Nature* **584**, 377-381 (2020).
48. Xu, C. *et al.* Two-dimensional antiferroelectricity in nanostripe-ordered In_2Se_3. *Phys. Rev. Lett.* **125**, 047601 (2020).
49. Zheng, C. *et al.* Room temperature in-plane ferroelectricity in van der Waals In_2Se_3. *Sci. Adv.* **4**, eaar7720 (2018).
50. Snedden, A., Knight, K. S. & Lightfoot, P. Structural distortions in the layered perovskites $CsANb_2O_7$ (A=Nd, Bi). *J. Solid State Chem.* **173**, 309-313 (2003).
51. Chen, C. *et al.* Ferroelectricity in Dion-Jacobson $ABiNb_2O_7$ (A = Rb, Cs) compounds. *J. Mater. Chem. C* **3**, 19-22 (2015).
52. Benedek, N. A. Origin of ferroelectricity in a family of polar oxides: the Dion—Jacobson phases. *lnorg. Chem.* **53**, 3769-3777 (2014).
53. Fennie, C. J. & Rabe, K. M. Ferroelectricity in the Dion-Jacobson $CsBiNb_2O_7$ from first principles.

Appl. Phys. Lett. **88**, 262902 (2006).
54. Heiland, G. & Ibach, H. Pyroelectricity of zinc oxide. *Solid State Commun.* **4**, 353-356 (1966).
55. You, L. *et al.* In-plane ferroelectricity in thin flakes of van der Waals hybrid perovskite. *Adv. Mater.* **30**, 1803249 (2018).
56. Chang, K. *et al.* Discovery of robust in-plane ferroelectricity in atomic-thick SnTe. *Science* **353**, 274-278 (2016).
57. Brehm, J. A. *et al.* Tunable quadruple-well ferroelectric van der Waals crystals. *Nat. Mater.*, in press (2019).
58. Fong, D. D. *et al.* Ferroelectricity in ultrathin perovskite films. *Science* **304**, 1650-1653 (2004).
59. Junquera, J. & Ghosez, P. Critical thickness for ferroelectricity in perovskite ultrathin films. *Nature* **422**, 506 (2003).
60. Mehta, R. R., Silverman, B. D. & Jacobs, J. T. Depolarization fields in thin ferroelectric films. *J. Appl. Phys.* **44**, 3379-3385 (1973).
61. Vilaplana, R. *et al.* Experimental and theoretical studies on α-In_2Se_3 at high pressure. *lnorg. Chem.* **57**, 8241-8252 (2018).
62. Liu, L. *et al.* Atomically resolving polymorphs and crystal structures of In_2Se_3. *Chem. Mater.* **31**, 10143-10149 (2019).
63. Xu, C. *et al.* Two-dimensional ferroelasticity in van der Waals β'-In2Se3. *Nat. Commun.* **12**, 3665 (2021).
64. Klemenz Rivenbark, C. F. *Liquid-phase epitaxy of advanced materials*. In *Springer handbook of crystal growth* (eds Govindhan Dhanaraj, Kullaiah Byrappa, Vishwanath Prasad, & Michael Dudley) 1041-1068 (Springer Berlin Heidelberg, 2010).
65. Morin, S. A., Forticaux, A., Bierman, M. J. & Jin, S. Screw dislocation-driven growth of two-dimensional nanoplates. *Nano Lett.* **11**, 4449-4455 (2011).
66. Lewis, B. The growth of crystals of low supersaturation: I. Theory. *J. Cryst. Growth* **21**, 29-39 (1974).
67. Guo, Y. *et al.* Unit-cell-thick domain in free-standing quasi-two-dimensional ferroelectric material. *Physical Review Materials* **5**, 044403 (2021).
68. Schilling, A. *et al.* Scaling of domain periodicity with thickness measured in $BaTiO_3$ single crystal lamellae and comparison with other ferroics. *Phys. Rev. B* **74**, 024115 (2006).
69. Taylor, D. Thermal expansion data. I: Binary oxides with the sodium chloride and wurtzite structures, MO. *Trans. j. Br. Ceram. Soc.* **83**, 5-9 (1984).
70. Pathak, P. & Vasavada, N. Thermal expansion of NaCl, KCl and CsBr by X-ray diffraction and the law of corresponding states. *Acta Crystallogr. A* **26**, 655-658 (1970).
71. Chynoweth, A. G. Dynamic method for measuring the pyroelectric effect with special reference to barium titanate. *J. Appl. Phys.* **27**, 78-84 (1956).
72. Lubomirsky, I. & Stafsudd, O. Invited review article: practical guide for pyroelectric measurements. *Rev. Sci. Instrum.* **83**, 051101 (2012).
73. Boehnke, U. C., Kühn, G., Berezovskii, G. A. & Spassov, T. Some aspects of the thermal behaviour of In_2Se_3. *J. Therm. Anal.* **32**, 115-120 (1987).
74. Wu, D. *et al.* Thickness-dependent dielectric constant of few-layer In_2Se_3 nanoflakes. *Nano Lett.* **15**, 8136-8140 (2015).
75. Newnham, R. E. *Properties of materials: anisotropy, symmetry, structure*. (Oxford University Press on Demand, 2005).
76. Langton, N. H. & Matthews, D. The dielectric constant of zinc oxide over a range of frequencies. *Br. J. Appl. Phys.* **9**, 453-456 (1958).
77. Jachalke, S. *et al.* The pyroelectric coefficient of free standing GaN grown by HVPE. *Appl. Phys. Lett.* **109**, 142906 (2016).
78. Lang, S. B. & Das-Gupta, D. K. *Chapter 1 - Pyroelectricity: fundamentals and applications*. In

Handbook of advanced electronic and photonic materials and devices (ed Hari Singh Nalwa) 1-55 (Academic Press, 2001).
79. Felix, P., Gamot, P., Lacheau, P. & Raverdy, Y. Pyroelectric, dielectric and thermal properties of TGS, DTGS and TGFB. *Ferroelectrics* **17**, 543-551 (1977).
80. Gebre, T., Batra, A. K., Guggilla, P., Aggarwal, M. D. & Lal, R. B. Pyroelectric properties of pure and doped lithium niobate crystals for infrared sensors. *Ferroelectr. Lett. Sect.* **31**, 131-139 (2004).
81. Beerman, H. P. Investigation of pyroelectric material characteristics for improved infrared detector performance. *Infrared Phys.* **15**, 225-231 (1975).
82. Tang, Y. *et al.* Composition, dc bias and temperature dependence of pyroelectric properties of 〈111〉-oriented $(1-x)Pb(Mg_{1/3}Nb_{2/3})O_3–xPbTiO_3$ crystals. *Mater. Sci. Eng. B* **119**, 71-74 (2005).
83. Sun, R. *et al.* Pyroelectric properties of Mn-doped $94.6Na_{0.5}Bi_{0.5}TiO_3$-$5.4BaTiO_3$ lead-free single crystals. *J. Appl. Phys.* **115**, 074101 (2014).
84. Liu, S. & Maciolek, R. Rare-earth-modified $Sr_{0.5}Ba_{0.5}Nb_2O_6$, ferroelectric crystals and their applications as infrared detectors. *J. Electron. Mater.* **4**, 91-100 (1975).
85. Zhao, Z. *et al.* Grain-size effects on the ferroelectric behavior of dense nanocrystalline $BaTiO_3$ ceramics. *Phys. Rev. B* **70**, 024107 (2004).
86. Yuzyuk, Y. I. Raman scattering spectra of ceramics, films, and superlattices of ferroelectric perovskites: A review. *Phys. Solid State.* **54**, 1026-1059 (2012).
87. Jehng, J. M. & Wachs, I. E. Structural chemistry and Raman spectra of niobium oxides. *Chem. Mater.* **3**, 100-107 (1991).
88. Link, A. *et al.* Temperature dependence of the E2 and A1(LO) phonons in GaN and AlN. *J. Appl. Phys.* **86**, 6256-6260 (1999).
89. Balkanski, M., Wallis, R. F. & Haro, E. Anharmonic effects in light scattering due to optical phonons in silicon. *Phys. Rev. B* **28**, 1928-1934 (1983).
90. Sun, X., Shi, J., Washington, M. A. & Lu, T.-M. Probing the interface strain in a 3D-2D van der Waals heterostructure. *Appl. Phys. Lett.* **111**, 151603 (2017).
91. Postmus, C., Ferraro, J. R. & Mitra, S. S. Pressure dependence of infrared eigenfrequencies of KCl and KBr. *Phys. Rev.* **174**, 983-987 (1968).
92. Ager, J. W., Veirs, D. K. & Rosenblatt, G. M. Spatially resolved Raman studies of diamond films grown by chemical vapor deposition. *Phys. Rev. B* **43**, 6491-6499 (1991).
93. Warren, B. E. *X-ray diffraction*. (Courier Corporation, 1990).
94. Liu, J., Fernández-Serra, M. V. & Allen, P. B. First-principles study of pyroelectricity in GaN and ZnO. *Phys. Rev. B* **93**, 081205 (2016).
95. Wang, B. & Gall, D. Fully strained epitaxial $Ti_{1-x}Mg_xN(001)$ layers. *Thin Solid Films* **688**, 137165 (2019).
96. Yuan, Y. *et al.* Three-dimensional atomic scale electron density reconstruction of octahedral tilt epitaxy in functional perovskites. *Nat. Commun.* **9**, 5220 (2018).

Methods

Liquid phase epitaxial growth of $CsBiNb_2O_7$ (CBNO) sheets. We chose $LaAlO_3$ (LAO) as the substrate for epitaxial growth of CBNO. The lattice mismatches between CBNO and LAO are about 4.1% for in-plane CBNO[100]‖LAO[100] with two CBNO unit cells matching three LAO unit cells and about 1.7% for in-plane CBNO[100]‖LAO[110] (obtained from the lattice parameters of orthorhombic CBNO, a=5.495 Å, b=5.423 Å, c=11.38 Å, and cubic LAO above 435 °C, a=3.821 Å). Prior to growth, we cleaned a LAO substrate (MTI Corporation) with acetone, ethanol and ultrapure water in an ultrasonic bath for 5 minutes successively and then blew it with dry air. CsCl (Sigma-Aldrich, 99.9%) is used as the molten salt and precursors include Cs_2CO_3 (Sigma-Aldrich, 99%), Bi_2O_3 (Sigma-Aldrich, 99.9%) and Nb_2O_5 (Sigma-Aldrich, 99.9%) with a molar ratio of 3:2:4. For the growth, we built up two setups: horizontal system (horizontal furnace) and vertical system (vertical furnace). The horizontal one is more convenient to grow small and thin sheets with a low weight ratio between the CsCl molten salt and precursors, while the vertical one is more effective to prepare big and thick sheets with a relatively high weight ratio. In the horizontal furnace setup, the LAO substrate was flatly placed at the bottom of a crucible and the weight ratio of molten salt to precursors was varied from 50:1 to 500:1. The temperature was increased to 200 °C and kept for 2 h to dry all powders. Then it was increased to 600 °C and kept for 2 h to decompose Cs_2CO_3 into Cs_2O. Subsequently, the temperature was increased to 900 °C, kept for 4 h and gradually decreased to room temperature with a cooling rate of 2 °C/min. In the vertical furnace setup, the LAO substrate was vertically placed and tied by a Pt wire. The weight ratio of CsCl molten salt to all precursors was varied from 10:1 to 50:1. The temperature was increased to 200 °C and kept for 2 h to dry all powders. After the decomposition of Cs_2CO_3 at 600 °C for 2 h, the temperature was increased to 850 °C for 4 h to fully melt all precursors and then suddenly decreased to 750 °C. Then the vertically hung LAO substrate lowed into the crucible and immerged into molten salt for 2 h. Finally, the LAO substrate was pulled out directly from the solution via the Pt wire, cooled down gradually to room temperature for further characterizations.

Pulsed laser deposition of ZnO thin films. We choose NaCl as the substrate for epitaxial growth of ZnO thin films. The lattice mismatch between ZnO and NaCl is 5.6% for in-plane ZnO[001]‖NaCl[100]. We obtained a fresh NaCl substrate by cleavage and then immediately loaded it into the growth chamber to avoid possible surface degradation. Prior to growth, the vacuum chamber was evacuated to about 10^{-5} mbar and then a O_2 gas flow (99.999%) was introduced into the chamber. A KrF excimer laser (wavelength of 248 nm) with a power of 150 mJ and a frequency of 5 Hz was used to ablate the ZnO target. We maintained the substrate temperature at 200 ˚C, 300 ˚C and 400 ˚C and pressure at about 5 mbar during the growth. We varied the growth time from 2 mins to 120 mins. Thus, ZnO epitaxial films with different thicknesses were fabricated.

Fabrication and transfer of freestanding sheets. To fabricate In_2Se_3 and CBNO sheets, we used a polydimethylsiloxane (PDMS) stamp to press a bulk In_2Se_3 crystal (HQ Graphene company) and an epitaxial CBNO/LAO sample, respectively, and then quickly removed the PDMS. Due to the layered nature of both In_2Se_3 and CBNO, sheets could be exfoliated and attached on the PDMS. To obtain ultrathin sheets, we pressed two PDMS stamps with thick sheets together and exfoliate a few times. Finally, we could transfer these sheets on any substrate by pressing the PDMS and then slowly removed it. The β'-In_2Se_3 sheets/crystals were obtained by annealing the α-In_2Se_3 sheets/crystals at 300 ˚C. To fabricate ZnO sheets, we first coated a poly (methyl methacrylate) (PMMA) film on the ZnO/NaCl sample as a supporting layer by spin coating. Then, we placed the PMMA/ZnO/NaCl sample in water. After the NaCl substrate was fully dissolved, we picked up the floating PMMA/ZnO film by using a Si wafer. Finally, a freestanding ZnO film was obtained after removing the PMMA layer by using acetone. By using a PDMS stamp, we can break the film into sheets and transfer the sheets onto any substrate.

Device fabrication. We used mask-less lithography (Intelligent Micro Patterning model SF-100 Lightning Plus, positive photoresist S1813) to draw patterns on a substrate (blue glass, an infrared (IR) absorber for pyroelectric measurements) with the channel distance of 10~30 μm. Then, we deposited Ti (3 nm)/Au (20 nm) layers on the patterned substrate by using e-beam evaporation. We used few-layer graphene (FLG) as electrical contacts. Few-layer graphene was fabricated by the same mothed for fabrication of In_2Se_3 sheets. We loaded the PDMS stamps with In_2Se_3 sheets, CBNO sheets, ZnO sheets or FLGs onto a 3-axis micro manipulator. Then we aligned the sheets to the Ti/Au patterned substrate under an optical microscope. Using the 3-axis micro manipulator, we gently attached the sheets onto the desired position and then gently released the PDMS stamp. After that, the sheets were left on the substrate. In this way, pyroelectric devices with FLGs as contacts were fabricated. For In_2Se_3, the polar direction is likely to be perpendicular to the edge of a triangle sheet. For CBNO, it is at 45 degrees with respect to the edge of a rectangle sheet. For ZnO, it is along [001] direction (one edge of the film). To ensure a polar component along the current direction, we aligned the channels of most CBNO-based and In_2Se_3-based devices to be roughly parallel to the edges of sheets and the channels of ZnO-based devices at about 45 degrees with respect to one edge of the film.

X-ray diffraction (XRD). We performed XRD measurements by using a Panalytical X'Pert PRO MPD system with a Cu Kα source and a PIXcel solid-state line detector. ω-2θ scans were acquired with a divergent beam Bragg-Brentano geometry over a large 2θ range from 5-90° in order to detect small inclusions of possible secondary phases or misoriented grains. ω-rocking curves were obtained using a constant 2θ angle corresponding to the CBNO 004 reflection and using a parallel beam geometry employing a hybrid mirror with a two-bounce two-crystal Ge(220) monochromator, yielding a parallel incident beam with a wavelength $\lambda_{K\alpha 1}$ = 1.5406 Å, a divergence of 0.0068°, and a width of 0.3 mm[95]. We obtained XRD pole figures and φ-scans by using a point focus optics with a poly-capillary X-ray lens that provides a quasi-parallel Cu Kα beam to minimize defocusing effects associated with the non-uniform sample height due to the sample tilt.

Synchrotron X-ay scattering: Synchrotron X-ray diffraction measurements of the CBNO single crystal sheet samples to quantitatively extract the Debye-Waller factor information were performed on a six-circle Newport Kappa diffractometer in the beamline 33-ID-D at Advanced Photon Source, Argonne National Laboratory[96]. The total X-ray flux is about 2.0×10^{12} photons s^{-1}. The X-ray beam was focused by a pair of Kirkpatrick–Baez mirrors down to a beam profile of ~ 20 μm (vertical) × 40 μm (horizontal) in order to collect sufficient diffraction signal out of the small size thin CBNO single crystal. The X-ray diffraction measurements were carried out using a X-ray energy of 20 KeV. The two dimensional diffraction images at the out-of-plane L direction in the reciprocal space were taken by a pixel array area detector (Dectris PILATUS 100 K). These images were used to properly remove the diffuse scattering background for data reduction. The temperature dependent X-ray diffraction measurements were performed an Anton-Parr Domed DHS-1100 heating stage mounted onto the Newport 6-circle diffractometer. The heating measurements were carried out in open air condition.

Microscopical characterizations. We characterized the morphology of sheets and films by using a Nikon Eclipse Ti-S inverted optical microscope. We used multi-mode TM atomic force microscope to check the flatness and obtain the thickness of sheets with a tapping mode. The high-resolution TEM image and electron diffraction pattern of CBNO sheet were collected with FEI F20 TEM operated at 200 kV. High-angle annular dark-field Cs-corrected scanning transmission electron microscopy (HAADF-STEM) images were acquired on a fifth-order aberration-corrected 300 keV FEI Titan Themis with a probe convergence semi-angle of 21.4 mrad and inner and outer collection angles of 68 and 340 mrad, respectively. We obtained vibration modes of the In_2Se_3, CBNO and ZnO sheets from Raman spectrum collected by using a Witec Alpha 300 confocal Raman microscope with an excitation source of CW 532 nm.

Second harmonic generation (SHG). We measured rotational anisotropy second harmonic generation (RA-SHG) by using a home-made system (Keopsys KPS-BT2-YFL-1083-40-COL 1083 nm 3 W CW fiber laser, Thorlabs 4 Megapixel Monochrome Scientific CCD Camera, Princeton Instruments SP-2358 spectrograph, and Nikon Ti-S optical microscope). We use a 1064nm 1/2 waveplate (Thorlabs, 25.4mm, Mounted Zero Order 1/2 Waveplate 1064nm) to rotate the polarization direction of our laser and a polarizer (Thorlabs, Visible Wire Grid Polarizers: 420–700 nm) to select the SHG signals with a polarization direction parallel to the (110) direction of a CBNO sheet.

Electron backscatter diffraction (EBSD). We performed EBSD to obtain spatial crystallographic orientation map, pole figure, and inverse pole figure. The detector is a NordlysNano detector from Oxford Instruments, integrated in a Karl Zeiss Ultra 1540 EsB SEM-FIB system. A 10 kV electron beam was used for the EBSD characterization, the sample was tilted at 70° relative to the incident electron beam with a working distance of 20.0 mm. The crystallographic orientation data was collected and analyzed by the Aztec software from Oxford Instruments. The surface scan area was set at 40×36 μm in size with a scan step of 1.0 μm.

Reflection high-energy electron diffraction (RHEED). For RHEED characterization of near surface structure of sheets, the CBNO sheets transferred on Si(100) substrate was loaded in a high vacuum chamber equipped with RHEED. The incident energy and incident angle of electron beam are 9 keV and ~1^{o}, respectively.

Transport measurements. For pyroelectric measurements of sheet-based devices, we used a periodic pulse technique. The IR laser beam was generated from a DILAS m1f4s22-1064 fiber coupled diode laser with a central wavelength of 1064 nm. The beam was focused by two long-focus convex lenses and the ×20 objective lens of optical microscope. A laser spot with diameter of ~100 μm was shone onto the micro device. To generate periodic heating cycles to induce the pyroelectric current, the laser beam was chopped at 133 Hz. A Stanford Research SR830 DSP lock-in amplifier onto which the chopper was connected as a reference signal was used to record the pyroelectric signal. To calibrate temperature at the substrate surface, we deposited a thin Ni stripe (~20nm) on the substrate and illuminated the stripe under the modulated IR laser. We connected a reference resistance with the Ni stripe in series. Then, we applied a stable voltage by using a Tektronix AFG1022 arbitrary function generator and measured the voltage of a reference resistance by using an oscilloscope (BK PRECISION 2190D). Thus, the resistance profile of the Ni stripe was obtained. Finally, the resistance profile was converted to temperature profile by a temperature coefficient of the Ni stripe measured by using a source meter and a heating stage. The temperature at the substrate surface is approximate to the temperature of the Ni stripe.

Molecular dynamics simulation. We designed a simple molecular model of hexagonal closed-packed (HCP) solid to understand the effect of interlayer bonding strength. There are six atomic species in this HCP model. Species A, B, C constitute hexagonally closed-packed *A* layer, while species D, E, F constitute the hexagonally closed-packed *B* layers, as shown in Supplementary Fig. 48a. Within each layer, atoms bond strongly to the other two species while repel the same species such that a monolayer hexagonal close-packed is thermodynamically stable, by the balance of the attractive intralayer hetero-bond and repulsive intralayer homo-bond. The interaction across layers is always attractive, varying from the intralayer hetero-bond strength (thus corresponding to bulk HCP crystal) to 1/2 of that. The particle-particle interaction is described by a modified Lennard-Jones (LJ) potential that we refer to as Bump Lennard-Jones (BLJ) potential:

$$\phi_{LJ}(r) = 4\varepsilon_{\alpha\beta}\left(\frac{\sigma_{\alpha\beta}^{12}}{r^{12}} - \frac{\sigma_{\alpha\beta}^{6}}{r^{6}}\right) - 4\varepsilon_{\alpha\beta}\left(\frac{\sigma_{\alpha\beta}^{12}}{r_{\alpha\beta,c}^{12}} - \frac{\sigma_{\alpha\beta}^{6}}{r_{\alpha\beta,c}^{6}}\right)$$

$$\phi_{BLJ}(r) = \begin{cases} \phi_{LJ}(r), & r < r_{\alpha\beta,s} \\ \phi_{LJ}(r) + \varepsilon_B \varepsilon_{\alpha\beta} \cdot sin^2\left(\pi \frac{r_{\alpha\beta,c} - r}{r_{\alpha\beta,c} - r_{\alpha\beta,s}}\right), & r_{\alpha\beta,s} \leq r < r_{\alpha\beta,e}. \\ \phi_{LJ}(r), & r > r_{\alpha\beta,e} \end{cases}$$

Here $\phi_{LJ}(r)$ is the conventional truncated LJ potential with $\varepsilon_{\alpha\beta}$ and $\sigma_{\alpha\beta}$ providing the energy and length scales and $r_{\alpha\beta,c}$ providing the cutoff. $\phi_{BLJ}(r)$ includes an additional energy penalty term between $r_{\alpha\beta,s}$ and $r_{\alpha\beta,e}$ with a bump height of $\varepsilon_B \varepsilon_{\alpha\beta}$. The potential parameter is shown in Supplementary Table 2. Supplementary Fig. 48b shows potential energy as a function of atomic separation for intralayer homo-bond (blue), intralayer hetero-bond (red) and interlayer bonds (green). The energy and length units are chosen as $\varepsilon_e = 0.5\varepsilon_{AB}$ and $\sigma_0 = \sigma_{AB}$ for convenience. All particles have identical mass of m_0. The time unit is $t_0 = \sigma_0\sqrt{m_0/\varepsilon_e}$. The equations of motion are numerically integrated using the velocity-Verlet algorithm with a time step of $0.005t_0$. The samples are between 10 to 32 layers in thickness. Each layer is about $0.91\sigma_{AB}$ in thickness. The lateral dimensions of the samples are about $67\sigma_{AB}$ by $68\sigma_{AB}$ with periodic boundary conditions. Initial structures are relaxed in Nose-Hoover isothermal isobaric ensemble to relax the in-plane stresses. Atomic displacement data was collected under canonical ensemble with the temperature of $0.15\ \varepsilon_{AB}/k$ controlled by a Nose-Hoover thermostat for a duration of 0.25M t_0. In-plane and total mean square displacements are calculated using the atomic positions from the second half (0.125M t_0) of the trajectory.

Data availability

All data related to this study are available from the corresponding author on reasonable request.

Acknowledgements

The work is supported by the Air Force Office of Scientific Research under award number FA9550-18-1-0116 and the NYSTAR Focus Center at Rensselaer Polytechnic Institute under award number C150117. This paper is also supported by the U.S. National Science Foundation [Platform for the Accelerated Realization, Analysis, and Discovery of Interface Materials (PARADIM)] under Cooperative Agreement No. DMR-1539918 and made use of the Cornell Center for Materials Research (CCMR) Shared Facilities, which are supported through the NSF MRSEC Program (No. DMR-1719875). We thank Jian Liu for the discussion on the mechanism of pyroelectricity.

Author contributions

J.S., J.J. and L.Z. conceived and developed the idea, and planned the experiments. J.J. and L.Z. prepared the samples, devices and performed optical, SEM and AFM measurements. L.Z., J.J. and Y.H. performed the pyroelectric measurements. H.Z. performed synchrotron XRD measurements. P.B. and Y.F.S. performed MD simulations. Y.H. performed SHG measurement. J.J. performed Raman measurements. Y.G. and J.J. performed TEM and STEM measurements. B.W. and R.J. performed XRD measurements. Z.C., S.P. and X.W. contributed to the experimental setups and crystal growth. Y.X. performed AFM measurements. Y.X. performed RHEED measurements. Z.L. performed EBSD measurements. J.J. and L.Z. processed the data and J.J., L.Z. and J.S. interpreted the results. J.J. and L.Z. wrote the initial draft. J.S. revised the manuscript. All the authors were involved in the discussion for data analysis. J.S. supervised the project.

Competing interests: the Authors declare no Competing Financial or Non-Financial Interests.

#: **Equally contributed authors**: J.J. and L.Z.

*: **Correspondence:** J.J.: jiangj2@rpi.edu; Y.F.S.: shiy2@rpi.edu; J.S.: shij4@rpi.edu